Article

The International Journal of Robotics Research
2021, Vol. 40(6-7) 895–922

DOI: 10.1177/02783649211002545
journals.sagepub.com/home/ijr

Biologically inspired electrostatic artificial muscles for insect-sized robots

Hongqiang Wang[1,2], Peter York[3,4], Yufeng Chen[5,6], Sheila Russo[7], Tommaso Ranzani[7], Conor Walsh[3,4], and Robert J. Wood[3,4]

Abstract

Millimeter-sized electrostatic film actuators, inspired by the efficient spatial arrangement of insect muscles, achieve a muscle-like power density (61 W kg^{-1}) and enable robotic applications in which agility is needed in confined spaces. Like biological muscles, these actuators incorporate a hierarchical structure, in this case building from electrodes to arrays to laminates, and are composed primarily of flexible materials. So comprised, these actuators can be designed for a wide range of manipulation and locomotion tasks, similar to natural muscle, while being robust and compact. A typical actuator can achieve 85 mN of force with a 15 mm stroke, with a size of $28 \times 5.7 \times 0.3$ *mm^3 and mass of 92 mg. Two millimeter-sized robots, an ultra-thin earthworm-inspired robot and an intestinal-muscle-inspired endoscopic tool for tissue resection, demonstrate the utility of these actuators. The earthworm robot undertakes inspection tasks: the navigation of a 5 mm channel and a 19 mm square tube while carrying an on-board camera. The surgical tool, which conforms to the surface of the distal end of an endoscope, similar to the thin, smooth muscle that covers the intestine, completes tissue cutting and penetrating tasks. Beyond these devices, we anticipate widespread use of these actuators in soft robots, medical robots, wearable robots, and miniature autonomous systems.*

Keywords

Bio-inspired robotics, millimeter-scale robots, electrostatic actuators, microfabrication

1. Introduction

Insect muscles possess numerous features that are desirable for actuators in similarly sized robotic systems. Their compliance allows them to be interwoven with rigid skeletal elements to generate complex motions and makes them robust to external disturbances. Their hierarchical structure, building from nanoscale myosin/actin molecules to microscale sarcomeres to macroscopic muscle fibers (see Figure 1), makes them highly scalable and controllable. Although it is possible to directly employ living cells or muscles for robotic actuation, challenges such as controllability and the need to provide metabolites to biological materials limit their utility at present (Ricotti et al., 2017; Sun et al., 2020; Webster-Wood et al., 2017). Alternatively, insights from biological muscle structure can be leveraged in order to achieve similar overall performance in artificial, robotic systems.

Scalable, high-performance actuation is of particular interest on the insect (i.e., millimeter) scale. Electromagnetic motors, which are ubiquitous in larger robots, are rigid, bulky, and relatively inefficient on the millimeter scale and are thus poorly suited to small-scale robots (Goldberg

[1]Shenzhen Key Laboratory of Biomimetic Robotics and Intelligent Systems, Department of Mechanical and Energy Engineering, Southern University of Science and Technology, Shenzhen, China
[2]Guangdong Provincial Key Laboratory of Human-Augmentation and Rehabilitation Robotics in Universities, Department of Mechanical and Energy Engineering, Southern University of Science and Technology, Shenzhen, China
[3]John A. Paulson School of Engineering and Applied Sciences, Harvard University, Cambridge, MA, USA
[4]Wyss Institute for Biologically Inspired Engineering, Harvard University, Cambridge, MA, USA
[5]Research Laboratory of Electronics, Massachusetts Institute of Technology, Cambridge, MA, USA
[6]Department of Electrical Engineering and Computer Science, Massachusetts Institute of Technology, Cambridge, MA, USA
[7]Department of Mechanical Engineering, Boston University, Boston, MA, USA

Corresponding authors:
Hongqiang Wang, Shenzhen Key Laboratory of Biomimetic Robotics and Intelligent Systems, Southern University of Science and Technology, 1088 Xueyuan Avenue, Shenzhen 518055, China.
Email: wanghq6@sustech.edu.cn

Robert Wood, Wyss Institute for Biologically Inspired Engineering, Harvard University, 29 Oxford Street, Cambridge, MA 02138, Cambridge, MA, USA.
Email: rjwood@seas.harvard.edu

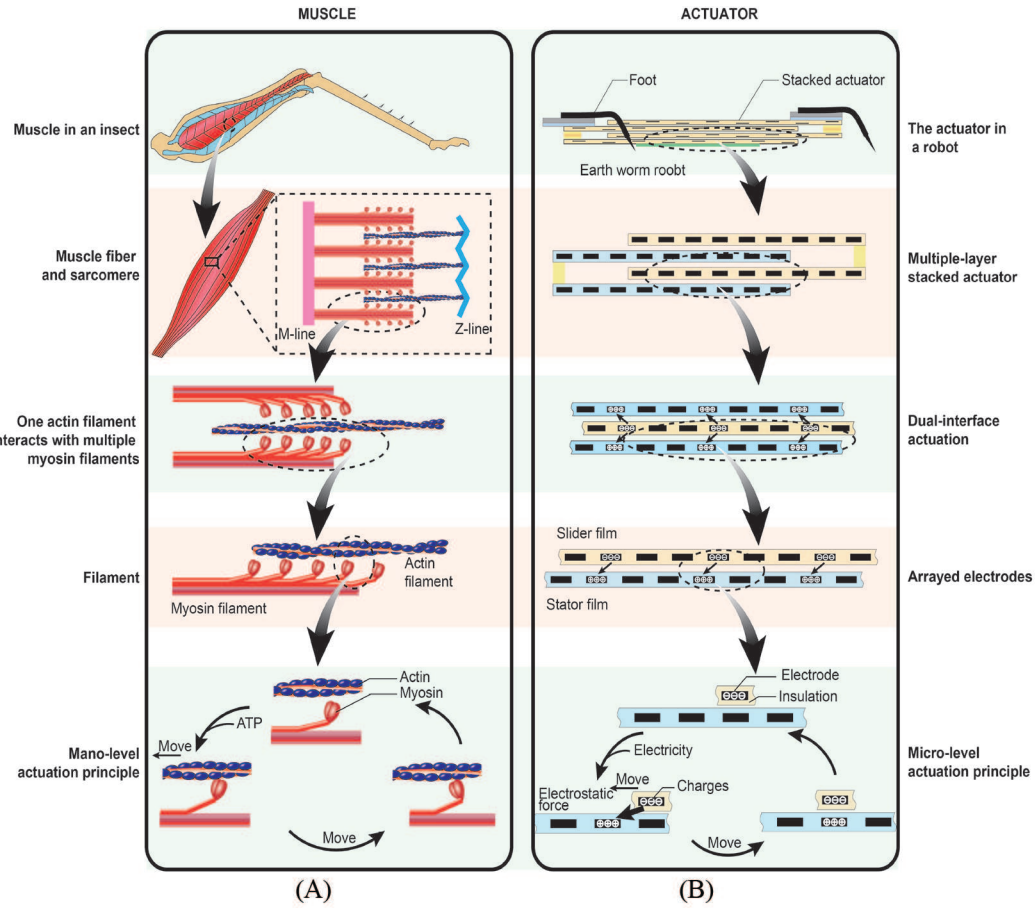

Fig. 1. The hierarchical structures of (A) skeletal muscle and (B) the electrostatic film actuator. At the smallest (nanometer) scale, actin and myosin molecules apply forces to generate a ratcheting motion. These actin and myosin molecules form a filament (each filament interacts with multiple filaments simultaneously in 3D space), filaments combine into a sarcomere, and consequently sarcomeres combine to form macroscopic muscles to power motion in animals. Similarly, in our electrostatic film actuator, at the micrometer level electrodes generate a driving force based on an applied electrostatic field. Multiple electrodes combine to form a film (each film interacts with upper and lower adjacent films simultaneously), multiple films form a stacked mesoscale actuator that is able to drive insect-sized robots.

et al., 2014; Madou, 2002; Trimmer, 1989). In pursuit of actuators better suited to the millimeter scale, researchers have developed many types that hew more closely to the soft material properties of natural systems. These so-called "induced-strain" actuators contract, expand, or bend when excited by an electrical signal and include piezoelectric actuators (Hassani and Tjahjowidodo, 2017; Li et al., 2017; Peng et al., 2015; Sun et al., 2017; York et al., 2017), shape memory alloys (SMAs) (Barbarino et al., 2014; Jani et al., 2014; Mulgaonkar et al., 2016; Sheng et al., 2017), ionic polymer–metal composites (IPMCs) (Jung et al., 2003), and dielectric elastomer actuators (DEAs) (Boys et al., 2017; Carpi et al., 2007; Gu et al., 2017; Lau et al., 2014; Nguyen et al., 2014). For each type, the stroke and force are governed by the geometry, material properties, and the applied electrical field or current. For these examples, however, the material stiffness is typically the most important factor and associated with the stroke of the actuator: stiff actuators tend to produce large stress but small displacement; compliant actuators produce low stress but large motions. Moreover, the viscoelasticity, creep, and hysteresis of the material during deformation results in non-linear characteristics and difficulties for precise control (Cordero et al., 2016; Kha and Ahn, 2006; Liu et al., 2017; Wood et al., 2005; Zou and Gu, 2018). These problems limit the contexts in which each type of induced-strain actuator can be reasonably used: none match the capabilities and adaptability of animal muscle, composed of muscle fibers that are coupled by a chemical ratchet-like mechanism instead of deformable materials as in induced-strain actuators.

This work aims to develop high-performance insect-sized artificial muscle using low-Young-modulus materials and a hierarchical structure, as suggested by natural muscle. The first step is to select a suitable driving mechanism. In this work we rely on electrostatic attractive forces, because electrostatic forces scale proportional to area and are thus well suited to millimeter-sized devices (Schindler et al., 2019; Trimmer, 1989). The second step in the hierarchical

design involves patterning individual electrode layers into power-dense arrays. This is particularly challenging at the millimeter scale owing to limitations with standard (e.g., photolithographic) fabrication and assembly techniques. Although several micro- and macro-scale actuators have been developed based on electrostatic forces (Bell et al., 2005; Cham et al., 2002; Chu et al., 1996; Grade et al., 2003; Legtenberg et al., 1996; Livermore et al., 2004; Martel, 2005; Penskiy and Bergbreiter, 2012; Rodgers et al., 2000; Tang et al., 1990, 1992, 2014; Tapuchi and Baimel, 2014; Yeh et al., 2002), only a few successful electrostatic actuators have been made at the millimeter scale (Chen et al., 2014; Minami et al., 1993; Schaler et al., 2018).

Building from prior designs, we focus on dry electrostatic actuators, because actuators depending on dielectric fluids suffer from evaporation in air and can freeze at low temperatures (although the output force can be greater owing to higher permittivity and dielectric strength of the dielectric fluid) (Kedzierski and Holihan, 2018; Niino et al., 1992, 1997a,b; Yamamoto et al., 1998, 2006). Most current electrostatic actuators at the microscale are based on comb structures, but their displacement is small (tens of micrometers, and less than 10% of the characteristic length of the actuator), as shown in Figure 2, which is ineffective for driving a millimeter-scale robot. Existing mesoscale (i.e., millimeter-sized) solutions try to overcome these challenges through the use of stroke-amplifying features (e.g., a zipper structure or a shuttle and clutch), but they sacrifice force output and structural complexity in doing so. In contrast, our millimeter-scale thin-film actuators, which fill the gap between micro- and macro-scale solutions, use a similar working principle to existing centimeter-sized electrostatic actuators: an electrostatic force between electrodes in the slider and the stator creates a net motion of the slider when the electrical signals to the electrodes are appropriately phased (Niino et al., 1992, 1997a,b; Wang and Yamamoto, 2013, 2017; Yamamoto et al., 1998, 2006). The principle is shown in Figure 3.

Based on this mechanism, we can implement the proposed actuator in a hierarchical structure, as shown in Figure 1. Electrodes in separate films can slide relative to each other when subjected to an electrostatic force. These electrodes are linearly patterned in films to multiply the actuation force, and two (or more) electrode films together create one actuator. The spatial efficiency can be enhanced by adding another electrode film, so the middle film can generate forces from fields from the two adjacent electrode layers, analogous to the arrangement in skeleton muscle where each myosin fiber interacts with multiple actin fibers and vice versa. By stacking more electrode films, the net force is amplified. The resulting actuator, with this hierarchical structure, is adjustable by tuning the number of electrodes and the actuation area. Similar to the fact that the insect muscle is different from vertebrate counterparts in many specific aspects (although the basic mechanism is the same) (Resh and Cardé, 2009), the design, fabrication, and assembly of mesoscale electrostatic film actuators cannot totally duplicate those of macroscopic electrostatic actuators. For example, the mass fraction of fastening and supporting elements can be up to 29% for macroscopic actuators (whereas the mass fraction of the electrode films are only 10%) (Egawa and Higuchi, 1990; Niino et al., 1994), which would be an unacceptable payload for a mesoscale robot. Moreover, in previous macroscopic stacked actuators, each electrode film only works in a single actuation interface because the cover layers on both sides of the film are different thicknesses. With these considerations in mind, there are three key challenges for creating efficient mesoscale electrostatic film actuators. First, the effective ratio and actuation force per area decreases rapidly as the size shrinks to several millimeters, because the nonactuation parts (e.g., micro-vias) cannot scale down proportionally and results in a reduced force. Second, the fabrication of smaller electrodes and interconnects between layers results in manufacturing difficulties, increased cost, and lower reliability (Holden, 2009; Ning, 2017; Pfahl et al., 2012). Finally, fixturing and assembly of the actuation films on the mesoscale is challenging, because common joining methods used in macroscopic systems, such as screws and nuts, are not practical at this scale, and larger assembly errors result in reduced output force.

To overcome these challenges, we turned to the insights gleaned from studying biological muscles across scales. For greater effective area and output force in a limited size, insect muscle, compared with vertebrate counterparts, has a different muscle arrangement (e.g., a higher thick-to-thin filament ratio) (King and Akai, 1982; Resh and Cardé, 2009), and fewer motorneurons. Thus, inspired by insect muscle, we redesigned the spatial pattern for higher spatial efficiency and reduced fabrication difficulties. In the new design, we utilize four phases of linear electrodes but slightly offset two of the phases to another plane to allow for wiring without vias and simultaneously match the number of conductive and insulation layers with previous macroscopic actuator designs, as shown in Figure 4. Without vias, the actuation area scales proportionally to the dimensions of the actuator. This configuration has the added benefit of decreasing the effective electrode pitch for a given space between electrodes in the same plane, and results in a higher maximum actuation force per area (approximately twice) for the same space (corresponding to the same maximum breakdown voltage). In addition, cost reduction is anticipated from the elimination of vias. The fabrication of vias includes steps of drilling, seeding, and electroplating. Typical fabrication materials and facilities are expensive (Keller, 2014; Lau and Chang, 2000); for example, a laser driller can cost more than US$500,000. Each step involves difficulties and possible failures. The reliability of vias is also reduced under mechanical strain, such as when the films are bent. Thus, without vias in the new pattern, fabrication yield is increased and costs are decreased. This resolves the second challenge of mesoscale electrostatic actuator creation, and

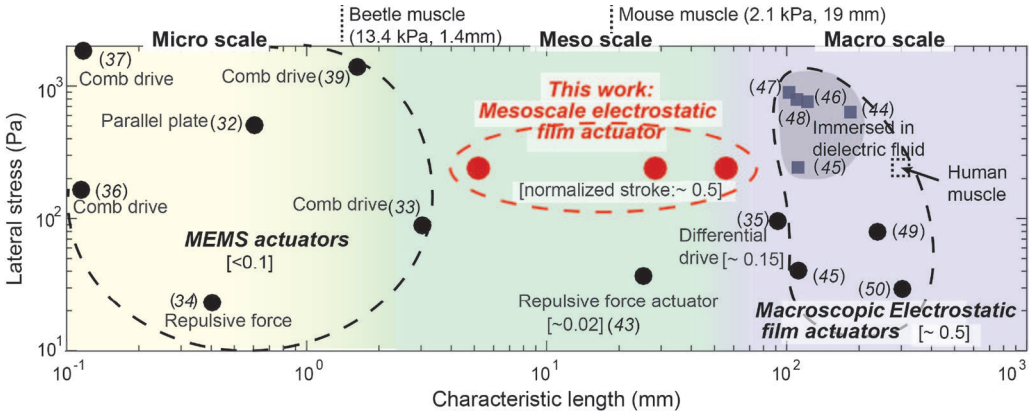

Fig. 2. Comparison of dry electrostatic actuators across different scales. The numbers in the square brackets indicate the actuator stroke (normalized by the characteristic length). The italic numbers in the parentheses indicate the following references in order: Chu et al. (1996), Yeh et al. (2002), Tang et al. (1992), Tang et al. (1990), Rodgers et al. (2000), Penskiy and Bergbreiter (2012), Tapuchi and Baimel (2014), Schaler et al. (2018), Niino et al. (1997a), Niino et al. (1997b), Niino et al. (1992), Yamamoto et al. (1998), Yamamoto et al. (2006), Wang and Yamamoto (2013), and Wang and Yamamoto (2017). Note that the data are estimated from figures if they are not reported explicitly. Muscle stress is also displayed as a reference, including beetle flight muscle (Josephson et al., 2000), mouse tibialis anterior (Burkholder et al., 1994; Gonzalez et al., 2000), and human tibialis anterior (Brand et al., 1986; Fukunaga et al., 1992).

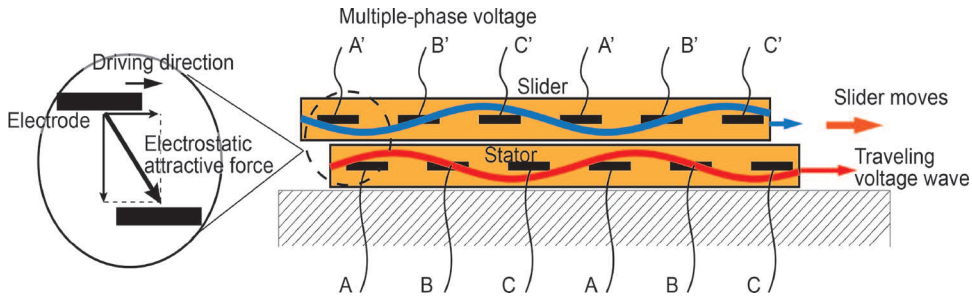

Fig. 3. Principle operation for our millimeter-sized electrostatic film actuators. The slider and stator films have identical structures. The electrodes are powered by multi-phase voltages.

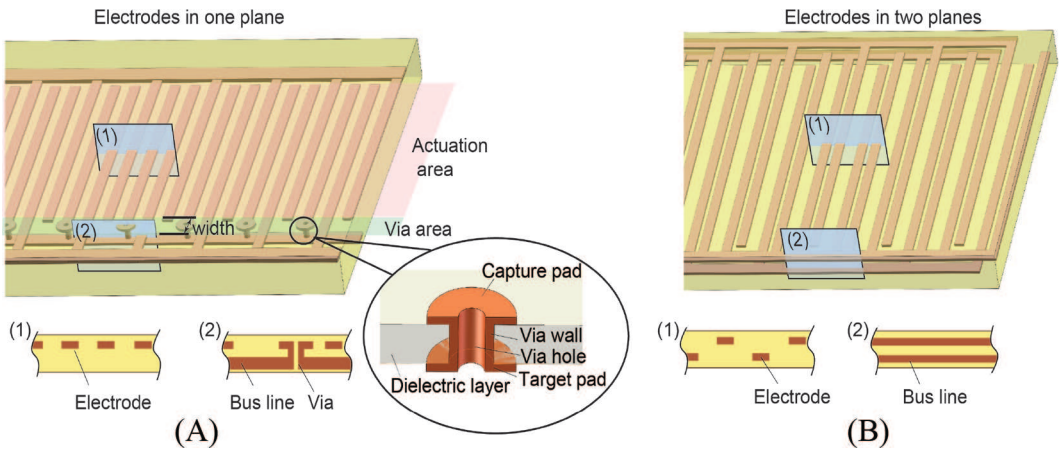

Fig. 4. Comparison between the electrode patterns. (A) Structure of the film with three-phase, one-plane electrodes used by existing centimeter-scale electrostatic film actuators, including (1) the cross section of the actuation area and (2) the cross section of the part with vias and bus lines. This design is difficult to manufacture on the mesoscale due to the need for vias. (B) Structure of the film with four-phase, two-plane electrode pattern that is proposed in this work. The cross sections with (1) the electrodes and (2) the bus lines are also represented respectively.

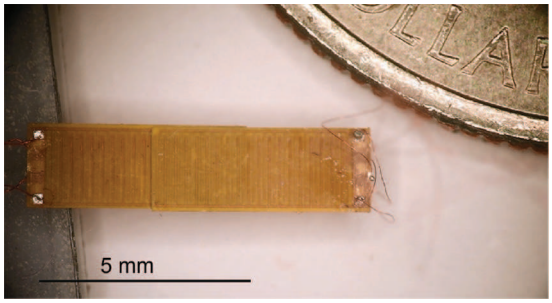

Fig. 5. An example prototype of the millimeter-sized electrostatic film actuators developed in this work, compared with a quarter dollar. See Extension 1.

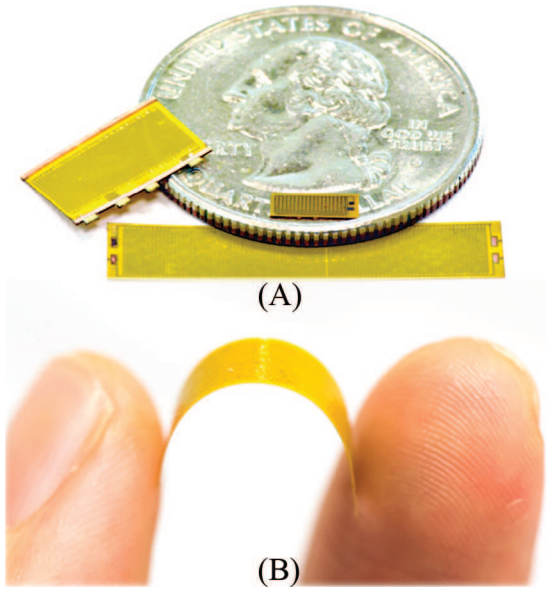

Fig. 6. Electrode films that constitute the layers of the actuators. (A) Electrode films of different sizes compared with a quarter dollar. (B) Flexibility of an electrode film.

leads into the solution for the third: because all the components are now distributed in 2D layers, the new pattern is more compatible with current high-precision micro/nanomanufacturing process such as laser ablation, photolithography, and soft lithography, and it has more potential to be mass produced by a roll-to-roll process to reduce cost further. To solve the problem of assembly and alignment of multiple layers, inspired by the combination of muscle filaments, we assemble the actuator films by bonding them on their edges, and develop two alignment methods (frame constraint and origami folding) for higher alignment accuracy. Based on these techniques, we devise a series of mesoscale electrode films and actuators, and one of them is shown in Figure 5 (see also Extension 1). Their sizes range from several millimeters to several centimeters. They are flexible because they are thin and composed of low-Young-modulus materials (see Figure 6). They exhibit high force-to-weight ratios (920 N kg^{-1}) and achieve large velocities (up to 224 mm s^{-1}), thus attaining muscle-like power-to-weight ratios (61 W kg^{-1}).

These actuators also possess certain qualitative properties desirable in robotic systems. Position and velocity control are accurate (micrometer level) and easy to implement owing to the fine pitch of the electrodes (tens of micrometers) and the synchronous actuation mechanism, in contrast with common actuation modalities (e.g., SMA and DEA) that cannot accurately control the instantaneous speed and displacement open loop. Based on their hierarchical structure, the actuators are scalable, with customizable properties based on the area or number of electrode layers. As the stator and slider are mechanically decoupled, unlike strain-induced actuators, the stroke can reach as high as 50% and is decoupled from material elasticity. Moreover, the electrodes and insulation layers of the electrostatic film actuators can be made from any conductive and non-conductive material, respectively, and thus there is a broad range of material options. For example, to reduce cost, we can use copper (US$6.9/kg, (Bloomberg, 2020)) for the electrodes and polyimide for insulation. Comparably, previous actuators (e.g., IPMC, SMA, and piezoelectric actuators) usually rely on specific and expensive materials, such as silver (US$780/kg), nitinol (US$180/kg), and lead zirconate titanate (US$131,000/kg) (Americanpiezo, 2020; Bloomberg, 2020; Hanz, 2020).

Based on these advantages, we incorporate our actuators into two mesoscale bioinspired robots, an ultra-thin earthworm robot and a modular endoscopic tool. The earthworm robot demonstrates the capability of completing inspection tasks such as navigating a 5 mm height channel and a 19 mm square tube while carrying an on-board camera. The flexibility of the films allows us to conform the flexible electrostatic artificial muscle to the profile of the distal tip of an endoscope. Although very thin, the surgical tool can complete tissue cutting and penetrating tasks. These demonstrations point to the broad use of this actuator in a wide variety of fields, exploration robots, medical robots, wearable robots, and miniature autonomous systems, with a promising future of achieving ubiquitous use on the millimeter scale.

2. Actuator design

To generate the actuator design, we began by examining the underlying physics. For any electrostatic actuator with a single slider and stator, the driving force is given by

$$F = \frac{\partial \mathbf{U}}{\partial x} = \frac{1}{2}\mathbf{V}^{\mathrm{T}}\frac{\partial \mathbf{C}}{\partial x}\mathbf{V} \tag{1}$$

where $\mathbf{U}$ is the stored electrical energy, $\mathbf{C}$ is the capacitance matrix (each element represents a capacitance between two different electrodes), x is the displacement of the slider, and $\mathbf{V}$ is the voltage vector, which contains the voltage applied to each phase of electrodes.

In the simplest case, an actuator only has one electrode in the slider and the stator, respectively. Each electrode is shaped as a plate, and hence (1) reduces to

$$F = \frac{1}{2}\epsilon A E^2 \tag{2}$$

where ϵ is the permittivity of the medium between the slider and stator, A is the effective electrode area, and E is the applied electric field. This model assumes that a change in slider position is proportional to a change in the distance between the two electrodes.

The relation shows two important results that are generalizable to more complex stator/slider electrostatic actuators: (1) that force scales with the area (in other words, force per area is scale-invariant), and (2) that the breakdown field of the gap medium bounds the maximum force that can be achieved (ignoring the non-linear effects that occur at gap sizes <10 μm, i.e., Paschen's law (Torres and Dhariwal, 1999)). Thus, decreasing the gap thickness will not result in a higher maximum force, though it will decrease the amount of voltage amplification needed to achieve that force.

Again examining Equation (1) and now allowing the single stator and slider electrodes to be of arbitrary geometry, we see that a large change in capacitance with slider position can be achieved if comb geometries are used; when the combs overlap, the capacitance is large, and when the combs are offset, the capacitance is small. Moreover, the change in capacitance with the slider position will be maximized if the distance between adjacent comb tines (i.e., the electrode pitch) is minimized.

The final key observation is that if multiple interwoven comb-shaped electrodes are used in the slider and the stator, continuous motion can be achieved by appropriately phasing the voltages of each electrode. Increasing the number of electrodes increases the smoothness of the resulting motion but also increases the complexity of the required drive electronics. To balance this tradeoff, three electrodes in both the stator and slider are typically used in previous electrostatic film actuators (Niino et al., 1992, 1997a,b; Wang and Yamamoto, 2013, 2017; Yamamoto et al., 1998, 2006), although other patterns such as two phases in the slider and four phases in the stator have also been developed before (Yamashita et al., 2007). In these patterns, all the electrodes are located in a single plane (Figure 4(A)). However, in one plane, only two phases of the electrodes can be directly connected to two bus lines, and the other electrodes can only make electrical connections by vias. Vias are the interconnections between two conductive layers. A typical structure is shown in Figure 4(A). The hole between the pads (the capture pad and target pad) of the two conductive layers can be drilled by mill or laser, and then coated with conductors by electroplating. The hole should be large enough to enable the deposition process (usually larger than 75 μm (Costello et al., 2013; Yen et al., 2012)). The two pads should be larger than the through hole to tolerate fabrication errors during drilling.

Given this understanding of the device physics, two problems with downs-scaling existing designs and achieving a large force output are evident: (1) it becomes increasingly difficult to minimize the electrode pitch as the minimum feature size of typical processes (screen printing, laser ablation, chemical etching, etc.) is reached; and (2) vias are difficult to scale down proportionally due to fabrication difficulties. Because vias do not contribute to force generation but require a finite space, the fraction of the actuator area that contributes to force generation decreases (Figure 7) (e.g., when the width of the via section is 475 μm, the actuation area is reduced by more than 20% of the total area if the actuator film is 2 mm wide and 4 mm long). Moreover, the hole drilling and plating processes for vias are more challenging than the fabrication of electrodes in a conductive layer, and hence the via holes and connection pads are usually much larger than the electrodes and space the manufacturer can make (Holden, 2009; Lau and Chang, 2000; Pfahl et al., 2012). For example, a typical printed circuit board (PCB) manufacturer can produce electrodes with pitches of approximately 50 μm, but their minimum available via holes and pads are 100 and 250 μm, respectively (Lau and Chang, 2000). As each via is surrounded by the electrodes, the space between electrodes should be large enough to leave enough area, but large spaces reduce the actuator force. Furthermore, the fabrication processes of micro vias, including drilling and plating, also increases the cost and decreases the efficiency of actuator fabrication. Plated vias bring more risk of failure to the actuators, because they are susceptible to delamination and electrical disconnection under bending and tension (Birch, 2009).

Our new electrode pattern, consisting of four phases of electrodes in both the slider and the stator, with two of them offset into different planes (Figure 4(B)), overcomes both of the aforementioned challenges of fabrication and scalability. First, by offsetting the electrodes, vias are no longer needed, increasing the useable area for actuation and, therefore, output force, as shown in Figure 7. Without vias, the associated manufacturing steps (drilling and plating holes) are avoided, and the cost decreases significantly.

Second, because the electrodes are split between planes, they can be packed closer together. This implies a smaller available electrode pitch (when the space is the same between electrodes in the same layer), which results in a larger maximum force output per actuation area (Figure 8). Note that while it is tempting to modify the single-plane design by reducing the electrode width to decrease the pitch (while holding the space between electrodes constant), this approach does not increase the output force, as shown in Figure 8. While comparing different patterns, it makes more sense to use the same spacing as a reference, rather than use the same pitch, considering the following two aspects. Actuators with similar electrode spacing will have a similar breakdown strength, which directly determines the maximum output force of the actuator. Moreover, the electrode feature size is directly governed by fabrication

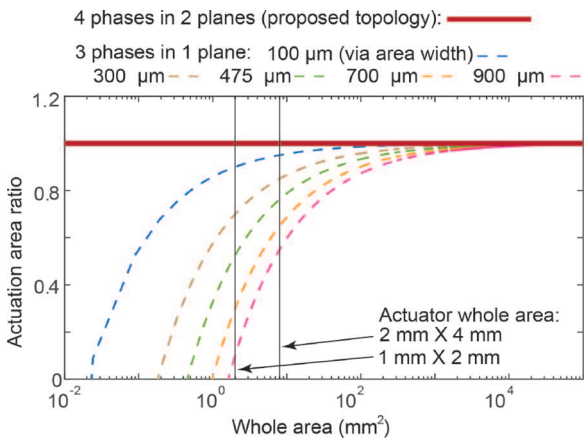

Fig. 7. Comparison of the theoretical actuation area ratio between our design and the previous approach. The length-to-width ratio of the actuator is assumed to be 2:1 and the area for bus lines is neglected. The width of the via area includes the pad diameter and space between electrodes.

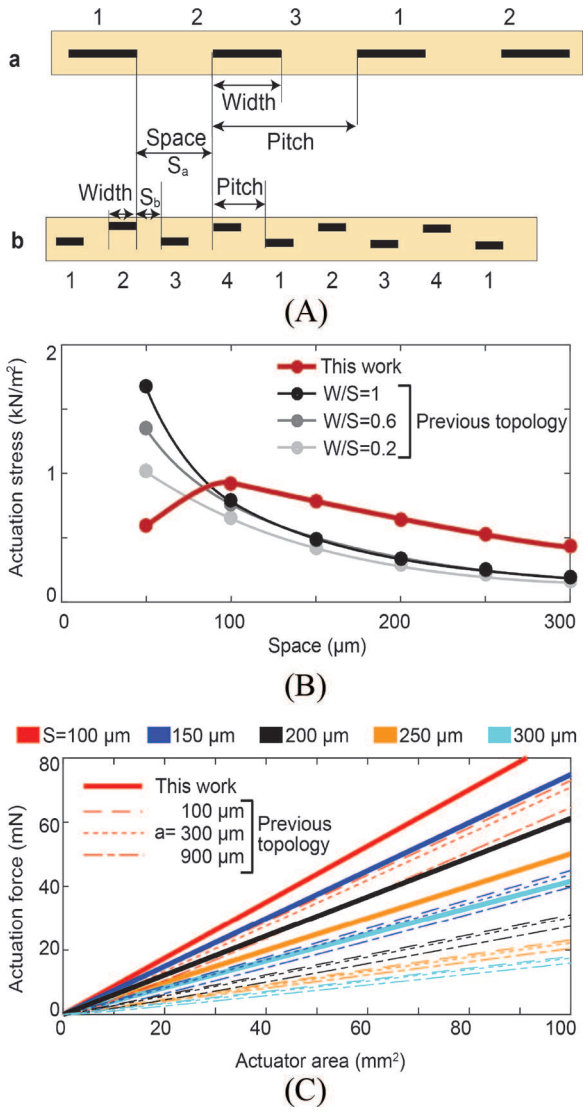

Fig. 8. Geometric definitions and the theoretical output force of our design compared with the standard approach. (A) Space and pitches for the pattern of (a) previous actuators (three-phase one-plane electrodes) and (b) the pattern of the actuators in this work (four-phase two-plane electrodes). (B) The theoretical output stress of our design compared with previous approaches, assuming the effective actuation areas are the same. W/S is the electrode width-to-space ratio. (C) The theoretical output force of our design compared with previous approaches, assuming the actuator areas are the same (a is the width of the via area). The voltage amplitude in the calculation is assumed to be 1 kV.

limitations. For example, in this work, the smallest space is limited by the effective laser kerf during ablation, while the pitch resolution is decided by the moving stage precision. As shown in Figure 8, when the spacing is smaller than 80 μm, although actuators using the previous patterns generate a stronger force than our design, they do not have sufficient space to include vias (via widths are typically larger than 100 μm (Lau and Chang, 2000). This is why the smallest pitch in previous work was 80 μm (Wang et al., 2012). When the spacing is larger than 80 μm, the actuators designed in this work can generate higher forces. This difference can be further enhanced if considering the effective actuation area caused by the vias. As shown in Figure 8(C), the actuators using the current design can generate twice the force of previous patterns for the same actuator areas.

The pattern of four phases is not the only choice for two plane electrodes, but it is the optimal choice. A detailed comparison and discussion can be found in the next section. As the actuator is driven by the electrostatic field between the electrodes on two films, one array of electrodes can contribute to the driving force on both sides of the film simultaneously, as shown in Figure 1, to increase the spatial efficiency and force/weight ratio of the actuator. Thus, we can stack multiple electrode films to generate a stronger force. The stator/slider films can be bonded on one edge, similar to the connection in insect muscles (Resh and Cardé, 2009) as shown in Figure 1.

3. Models and analyses

3.1. Mathematical model

For a four-phase actuator, we can use symmetry to reduce the full expression for output force (Equation (1)) into a more manageable form. The full voltage vector is given by

$$\begin{aligned}\mathbf{V} = [&V_{\mathrm{st}} \sin(2\pi f_{\mathrm{st}} t) \quad V_{\mathrm{st}} \sin(2\pi f_{\mathrm{st}} t + \pi/2)\\ &V_{\mathrm{st}} \sin(2\pi f_{\mathrm{st}} t + \pi) \quad V_{\mathrm{st}} \sin(2\pi f_{\mathrm{st}} t + 3\pi/2)\\ &V_{\mathrm{sl}} \sin(2\pi f_{\mathrm{sl}} t) \quad V_{\mathrm{sl}} \sin(2\pi f_{\mathrm{sl}} t + \pi/2)\\ &V_{\mathrm{sl}} \sin(2\pi f_{\mathrm{sl}} t + \pi) \quad V_{\mathrm{sl}} \sin(2\pi f_{\mathrm{sl}} t + 3\pi/2)]'\end{aligned} \tag{3}$$

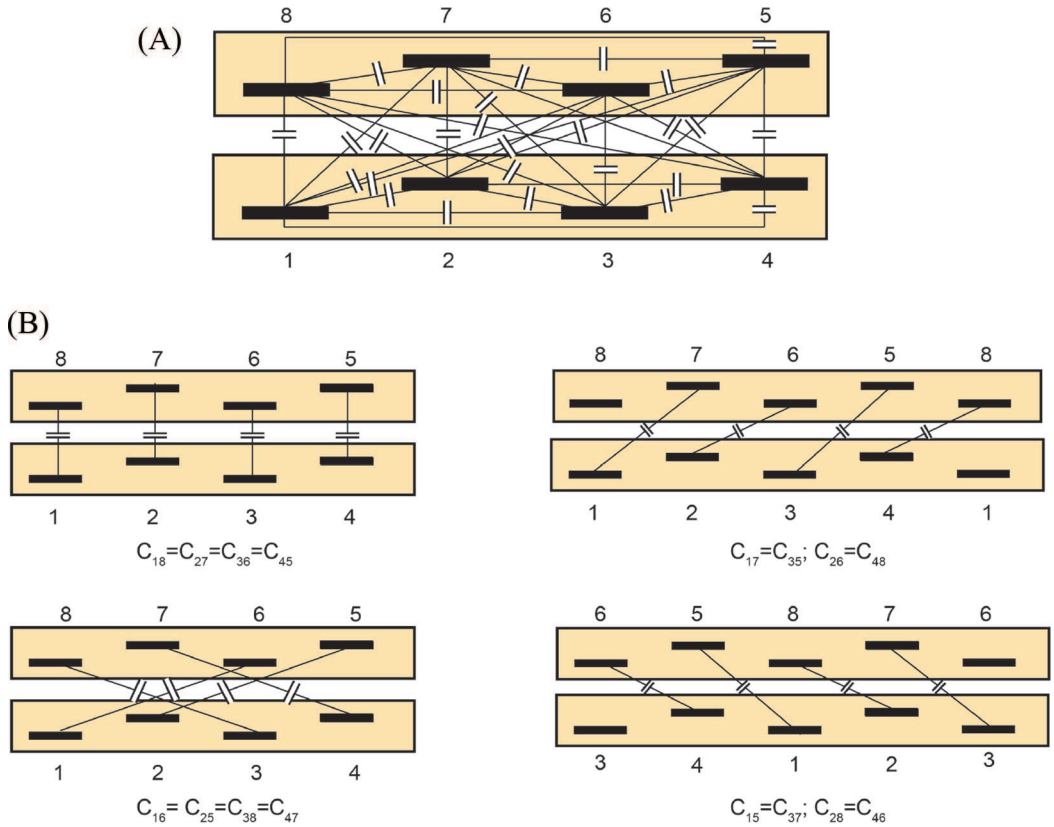

Fig. 9. Capacitance matrix in an actuator with four-phase two-plane electrodes. (A) All the capacitance terms. (B) Relationship of the capacitances between electrodes in different films.

where V_{st} and V_{sl} represent the amplitude of the AC voltage on the electrodes in the stator and slider, respectively, and f_{st} and f_{sl} are the driving frequencies of the stator and slider, respectively. With no loss of performance, we can supply the same set of four-phase voltages to the two films of the actuator and, hence, we set $V_{st} = V_{sl} = V$ and $f_{st} = f_{sl} = f$. We define the excitation phase (ϕ) to be $\phi = 2\pi f_{st}t = 2\pi f_{sl}t$

The elements (C_{ij}) of the capacitance matrix, which are functions of geometry, material properties, and slider position, are more complex. They can be calculated via finite element analysis (FEA), after which several symmetries can be identified and simplifications made. First, the change of each capacitance element in a single film (e.g., C_{12} and C_{56}, as shown in Figures 9 and 10) is negligible. Second, elements corresponding to capacitances between electrodes in two different films can be approximated by cosine functions of the slider displacement. Some of these elements are nearly the same (e.g., the amplitude difference between C_{17} and C_{26} is 6% in the model described in this work), several elements have similar amplitudes but different phase offsets (e.g., the amplitude difference between C_{16} and C_{18} is 10%, and the phase shift is π), and others have the same phase offset but different amplitudes (e.g., the amplitude difference between C_{18} and C_{27} is 65%). Recognizing all of these simplifications, the elements (C_{ij}) can be written as

$$C_{ij} = \begin{cases} C_{18} = C_{36} = C_{m0} + C_{m1}\cos\left(\frac{\pi x}{2p}\right) \\ C_{27} = C_{45} = C'_{m0} + C'_{m1}\cos\left(\frac{\pi x}{2p}\right) \\ C_{17} = C_{26} = C_{35} = C_{48} = C''_{m0} + C''_{m1}\cos\left(\frac{\pi x}{2p} + \frac{\pi}{2}\right) \\ C_{16} = C_{38} = C_{m0} + C_{m1}\cos\left(\frac{\pi x}{2p} + \pi\right) \\ C_{25} = C_{47} = C'_{m0} + C'_{m1}\cos\left(\frac{\pi x}{2p} + \pi\right) \\ C_{15} = C_{28} = C_{37} = C_{46} = C''_{m0} + C''_{m1}\cos\left(\frac{\pi x}{2p} + \frac{3\pi}{2}\right) \end{cases} \quad (4)$$

where p is the electrode pitch, C_{m0}, C'_{m0}, and C''_{m0} are mean values, and C_{m1}, C'_{m1}, and C''_{m1} are the amplitudes (which can be calculated via Fourier analysis). These values can be found at a discretized set of slider positions and then can be used to calculate the force of the actuator at different positions and excitation phases by Equation (1). As shown in Figure 11, if the payload is smaller than the maximum capacity of the actuator, the actuator can always find a sequence of parameter sets (the positions and excitation phases) to balance the payload and remain synchronous.

The output force can be amplified by stacking more films together. In a stacked actuator, all film-on-film interfaces contribute to electrostatic force generation. If there are N films in a stacked actuator, and each actuation interface

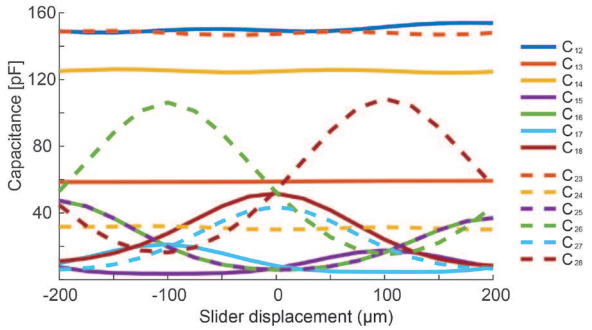

Fig. 10. Capacitances at different displacements in the FEA model. The results are for the four-phase two-plane design when the pitch is 100 μm.

generates the same force F_{dr}, then the total force generated is

$$F_{stack} = (N-1)F_{dr} \tag{5}$$

Assuming each electrode film has a mass W, and the maximum output power of each actuation interface is P_{max}, the total power density is

$$P_{stack} = \frac{(N-1)P_{max}}{NW} \tag{6}$$

This implies that the power density is lowest $P_{max}/(2W)$ when the actuator contains only two films, and this ratio increases and tends to P_{max}/W as more electrode films are added to the actuator.

As the actuators operate synchronously, their speed is proportional to the driving frequency (Niino et al., 1997a),

$$v = 8pf \tag{7}$$

which is verified experimentally. This relation holds regardless of external loading, provided the external load is below the actuator's blocked force. Hence, the actuator's motion can be controlled easily without the addition of displacement/speed sensors

3.2. *Finite element model*

For a given actuator design, the capacitance matrices at different slider positions were derived using FEA, which we conducted using commercially available software (COMSOL Multiphysics 4.4). The slider and stator were bounded by an air-filled box, the walls of which were treated as infinite elements with zero charge to simulate an infinite boundary condition. The air gap between the two films was assumed to be 15 μm, in accordance with preliminary trials. The thickness and permittivity of each layer are listed in Table 1 according to the materials and fabrication methods used in this work, and a sample image showing the mesh and the modeled electric field is shown in Figure 12. The model was solved by applying a voltage to each electrode in turn and calculating the charge on each other electrode. This gave the capacitance matrix at the initial slider position; then, sweeping through a period of the rotor's motion using a discretized set of positions (we found 17 to be appropriate) the capacitance matrix throughout the slider's trajectory was acquired.

Table 1. Specification of the FEA model for the actuators.

Layer	Thickness (μm)	Material	Relative permittivity
Cover layer	7.5	Kapton film	3.4
Bonding layer	25	Acrylic adhesive	3.5
Electrode layer	5	Copper	—
Air gap	15	Air	1

The largest source of error in the model is likely to be some relatively minor fringing effects. Six sets of electrodes were determined to be a suitable number in order to mitigate the effects of in-plane fringing while keeping the model relatively simple. We found that increasing the number of electrode sets to 20 resulted in a relatively minor change (approximately 10%) in the simulation results. Our model does not, however, capture any out-of-plane fringing, as it is a 2D model.

3.3. *Comparison of different patterns*

In this research, we propose to arrange the electrodes in multiple planes and phases to avoid micro-vias, simplify fabrication, and increase the maximum output force. Here we discuss and compare four patterns: three-phase electrodes in one/two planes and four-phase electrodes in one/two planes. Other patterns with more electrodes or planes could be compared based on the calculation methods that follow, but more electrodes require more power supplies for little gain in performance and more electrode planes result in increased fabrication challenges, so we exclude those topologies from the current comparison.

Of the four patterns under consideration, the pattern with three-phase electrodes in two planes can be discarded immediately. Compared with the patterns with electrodes in one plane, one-third of their electrodes are further from the actuation interface, and hence the output force is weaker. Moreover, the space between electrodes in the same plane is equal to the electrode width, while the patterns with four phase electrodes in two planes can use spacing much greater than the electrode width, which implies much easier fabrication.

Now we briefly compare the remaining three patterns: four-phase electrodes in two planes and three or four electrodes in one plane. We consider two key metrics for comparison: actuation area ratio and driving force. First, the film with four-phase electrodes in two planes has an actuation area ratio that is scale-invariant, while for the film with three/four-phase electrodes in one plane (usually utilized in macroscopic electrostatic actuators (Niino et al., 1992,

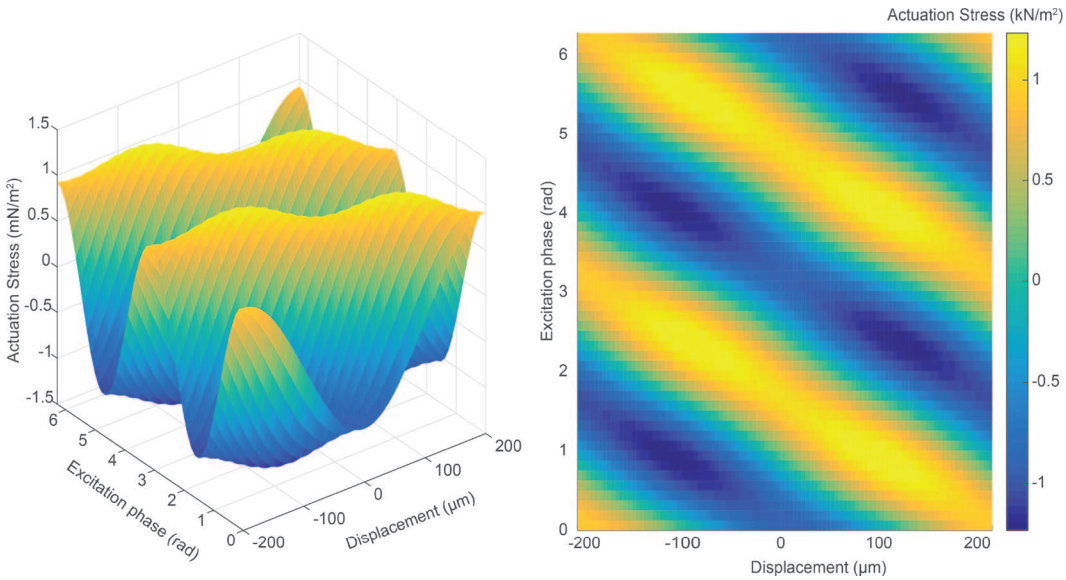

Fig. 11. The force at different displacement phases and excitation phases in an actuator with four-phase two-plane electrodes. The values on the ridge of the data represent the maximum output force of the actuator at particular positions. We choose the minimum value on the ridge as the maximum output force of the actuator. The voltage amplitude is 1 V_{0-p} and the pitch is 100 μm.

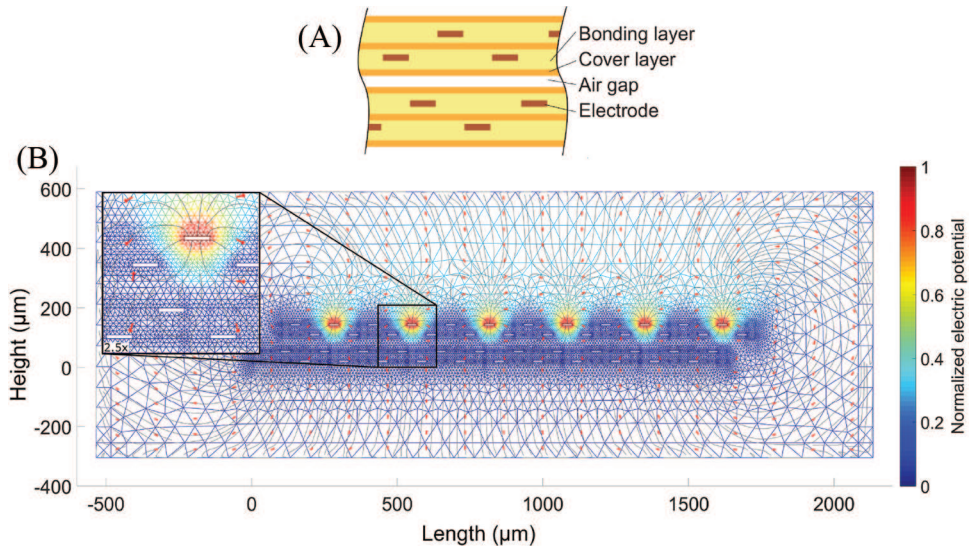

Fig. 12. The FEA model for the analysis of the electrostatic actuators in this work. (A) Schematic of the model. (B) Field distribution of the model as the slider moves 100 μm (67 μm pitch).

1997a,b; Wang and Yamamoto, 2013, 2017; Yamamoto et al., 1998, 2006)) this is not true owing to the vias. To facilitate hole drilling and electroplating, the via hole diameter and the corresponding connecting pads should not be too small, and to avoid electrical breakdown, a minimum gap between connection pads and other electrodes (as shown in Figure 4) should also be maintained. For instance, in a film with three/four-phase electrodes on one plane, as the length of the film becomes tens of centimeters, the actuation area ratio will be nearly 100%, and the area for vias can be neglected. However, if the length of the actuator shrinks to several millimeters, the actuation area will fill approximately 0–50% of the whole film area (see Figure 7). Although the micro-vias can scale down to some extent, the failure ratio and fabrication costs increase. For comparison, the actuation area in a film with four-phase electrodes on two planes will not vary. Therefore, the pattern with four-phase electrodes in two planes is the favorable option with regards to scalability.

To compare the maximum output force for different patterns, we assume that they have the same actuation area and the same space width between electrodes (and, thus, the same breakdown voltage) in the following analyses. The pattern with four-phase two-plane electrodes has two

dimensions that can be referred to as spaces: the space between electrodes in the same plane (S_a) and the space between two electrodes in different planes (S_b) as shown in Figure 8. Here we need to clarify which is suitable for the comparison to other patterns, and which parameter determines electrical breakdown. In-plane electrodes are more subject to shorting because the space between electrodes in the same plane is closer to the air, and the dielectric strength of air is approximately 1% of the dielectric strength of most polymers (e.g., air 3 kV mm^{-1}; polyimide 300 kV mm^{-1}) (Diaham et al., 2010; Peek, 1911). Therefore, we can compare the maximum force of the actuators with four-phase two-plane electrodes based on the in-plane space S_a. Given that S_a is half of the pitch, in the pattern with four-phase two-plane electrodes, S_a can be 3/2 times of the pitch, whereas the patterns with three/four electrodes in a single plane have S_a equal to half of the pitch. This means that, if the spacing is the same, the pitch of the actuator with four-phase two-plane electrodes is only one-third of that of the actuators with one-plane electrode patterns. Hence with the same spacing (i.e., the same breakdown voltage), the two-plane pattern can achieve a higher density of electrodes. Therefore, the actuator with four phase electrodes in two planes can yield a stronger maximum force, as shown in Figure 8, unless its pitch is too small. There is an optimum value of the spacing in this case: when the space is 100 μm (pitch 66.6 μm), the output force is maximum. Once the spacing is smaller than this value, the output force will plummet, because the electrodes are too close so that they interfere with each other. Therefore, we designed the pitch of the actuator to be 66.6 μm.

3.4. *Effects of fabrication and assembly errors*

During fabrication and assembly, errors are inevitable. This section aims to clarify how manufacturing and assembly errors affect the output force, along with possible mitigating solutions. In this work, we mainly assess the effects of two dominant errors: (A) the misalignment between electrode planes inside a film; and (B) the misalignment between stator films (or slider films), as shown in Figure 13. For simplicity, in the computation of the following cases, the pitch of electrodes is 100 μm, and the other parameters are listed in Table 1.

3.4.1. Misalignment of electrodes in the same film. In a single-electrode film, there are two planes of electrodes. The alignment error inside a plane is due to the electrode fabrication process (e.g., laser ablation in this work), which is usually negligibly small (less than several micrometers), whereas the misalignment of the electrodes between the two planes is larger due to the manual assembly process. Here we assume the electrode offsets between planes in the slider and stator are $\Delta x'$ and $\Delta x''$, respectively, as shown in Figure 13. Then the elements of the capacitance matrix are given by

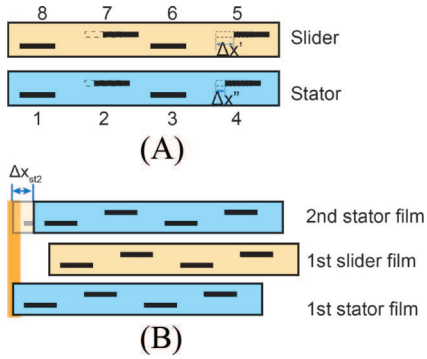

Fig. 13. The misalignment (A) between electrodes in the same film and (B) between electrodes in different films.

$$C_{ij}^{*} = \begin{cases} C_{18}^{*} = C_{36}^{*} = C_{18}(x) \\ C_{27}^{*} = C_{45}^{*} = C_{27}(x + \Delta x' - \Delta x'') \\ C_{17}^{*} = C_{35}^{*} = C_{17}(x + \Delta x') \\ C_{26}^{*} = C_{48}^{*} = C_{26}(x - \Delta x'') \\ C_{16}^{*} = C_{38}^{*} = C_{16}(x) \\ C_{25}^{*} = C_{47}^{*} = C_{25}(x + \Delta x' - \Delta x'') \\ C_{15}^{*} = C_{37}^{*} = C_{15}(x + \Delta x') \\ C_{28}^{*} = C_{46}^{*} = C_{28}(x - \Delta x'')) \end{cases} \tag{8}$$

If we assume that the amplitudes C_{m1}, C'_{m1}, and C''_{m1} do not change as the electrode offsets, their values can be computed from the same finite element model mentioned in Section 2.2. Based on Equations (1) and (8), we can calculate the output force of actuators for different offsets, and the results are shown in Figure 14. When the electrode plane offsets in either the stator or slider, the force decreases, and if the offsets in the slider or stator are approximately two-thirds of the electrode width, the output force drops by 10% of the initial value. Hence, for maximum output force, the assembly of the electrode planes in the same film should be careful to guarantee the offsets are smaller than two-thirds of the electrode width. In this work, we employ alignment holes and pins to precisely align the electrodes in different planes, as explained in the next section.

3.4.2. Misalignment of electrodes in different films. In a stacked actuator, the films are piled upon each other. If there is misalignment between the stator films (or slider films), as shown in Figure 13(B), the actuation interfaces cannot generate exactly the same force simultaneously because the force varies with respect to the relative position of the slider and stator as aforementioned. The net force of an actuator containing n films can be described by

$$F = \sum_{i=1}^{n-1} F_i - F_f \tag{9}$$

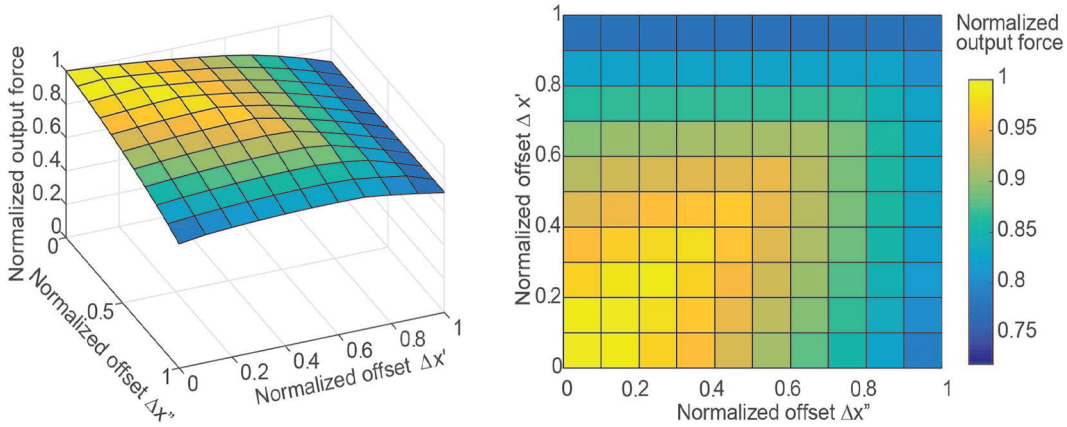

Fig. 14. The maximum output force of actuators with misaligned electrodes in different planes. The slider film offset is normalized by the space between the neighboring electrodes on two planes. The force is normalized by the maximum value.

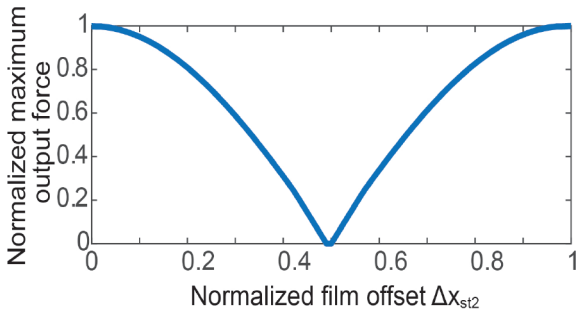

Fig. 15. The maximum output force of actuators with misalignment between films in a mesoscale electrostatic film actuator. The slider film offset is normalized by four pitches. The force is normalized by the maximum value.

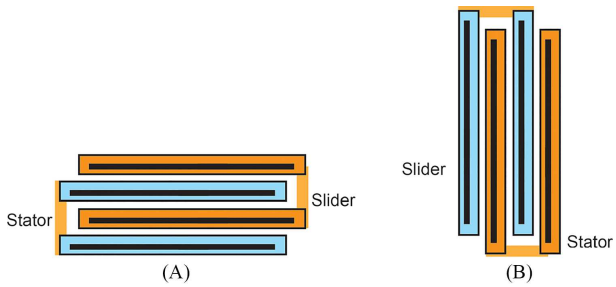

Fig. 16. Two film arrangement forms for electrostatic film actuators. (A) Horizontal arrangement. (B) Vertical arrangement.

where F_i is the force of the ith sub-actuator in the stacked layers, and F_f is the net friction force. The force of each sub-actuator can be expressed by

$$F_i = \begin{cases} F\left(x + \Delta x_{sl\frac{i+1}{2}} - \Delta x_{st\frac{i+1}{2}}\right) & \text{if } i \text{ is odd} \\ F\left(x + \Delta x_{sl\frac{i}{2}} - \Delta x_{st\frac{i+2}{2}}\right) & \text{if } i \text{ is even} \end{cases} \tag{10}$$

where Δx_{sli} and Δx_{sti} are the offsets of ith slider and stator, respectively. As the first stator and slider are the position reference, we need to satisfy $\Delta x_{sl1} = \Delta x_{st1} = 0$. Here, for simplicity, we analyze an actuator consisting of three stacked films (two actuation interfaces). The normalized force is shown in Figure 15. When the offset of the third film is close to two pitch lengths, the output force becomes zero, and the peak force appears when the offset is approximately four times the pitch. To guarantee the force is at least 90% of the maximum value, one should make the offset less than 0.6× the pitch. In this work, we developed two methods to eliminate the offset, and the details can be found in the next section.

The net friction force of the actuator can be expressed by the following equations:

$$F_f = \begin{cases} \mu_1 \frac{(n-1)n}{2} m_0 g & \text{horizontally arranged} \\ \mu_2 n m_0 g & \text{vertically arranged} \end{cases} \tag{11}$$

where μ_1 and μ_2 are the coefficients of the friction on the interfaces, m_0 is the mass of an electrode film, and g is the gravitational constant. Note that $n \geq 2$. The horizontal and vertical arrangements are depicted schematically in Figure 16.

According to this equation (assuming μ_1=μ_2), when n=2, the friction force for horizontal arrangement is smaller than that for vertical arrangement; when n=3, the friction forces are the same for the two arrangements. When n>3, the friction force for the horizontal arrangement becomes greater than that for the vertical arrangement. When n is small, the influence of friction can be neglected because the electrode films are low mass. For example, in our case, in Actuator 7, four films result in a friction force of only 0.14 mN, considerably smaller than the driving force (85 mN at 500 V). According to the above equation, F_f is proportional to n for the vertical arrangement, and to the square of n for the horizontal arrangement. This means the actuation force is always larger than the friction force for the vertical

arrangement. Conversely, for the horizontal arrangement, the friction force can be greater than the net friction force when n is very large. For instance, in the actuator composed of Film A (the coefficient of friction is assumed to be 0.1), only when the films are more than 2,669 layers does the friction force become stronger than the actuation force. When n is so large, the films can be vertically arranged. The area of the electrode films influences the actuation force and friction force simultaneously at the same rate and, hence, the net driving force is proportional to the area. In the discussion given previously, the friction force is only considered to be generated by gravity. In practice, however, many other aspects induce friction. For example, the pre-stress between the films owing to the deformation of the films can be another possible contribution to the normal force.

4. Fabrication and assembly

4.1. Fabrication of the electrode films

An overview of our fabrication process, which is derived from printed circuit microelectromechanical system (MEMS) techniques (Whitney et al., 2011), is shown in Figure 17. First, a piece of thin copper foil (5 μm; MicroThin, Mitsui Kinzoku) is bonded to a glass slide using a double-sided adhesive pad (WF film 0, Gel-Pak) and a single-sided adhesive pad (WF film 8, Gel-Pak). The electrode pattern in the copper is then ablated by a 355-nm DPSS laser micromachining system (Oxford Lasers E Series). The single-sided adhesive pad is used to avoid warping the copper electrode as it is heated by the laser. To ensure accurate ablating of the electrodes, we use a single pass at 10 mm s^{-1} and 0.52 W laser power. After ablating the electrodes, we remove the unwanted copper and peel off the single-side adhesive pad. By repeating these two steps, we can create an additional layer of electrodes. These two layers of electrodes are then bonded together by two pieces of heat-curable acrylic adhesive film (13 μm, FR1500 Pyralux) and a 7.5 μm thick polyimide film (Kapton) using a heat press (200°C, 1.33 MPa, 2 hours). To achieve accurate alignment between layers, we place dowel pins in precision-machined holes in a custom fixture, using fiducial holes laser-machined into the film layers. To guarantee uniform pressure during curing, we stack four pieces of rectangular supporting sheets on both the top and bottom sides: a Teflon film (0.5 mm), a compressible paper pad (0.6 mm), stainless steel foil (0.1 mm), and a hard rubber sheet (0.8 mm) (in order from the inner to the outer surfaces). After the acrylic adhesive is cured, the adhesive pads of the two sides are peeled off. Lastly, another acrylic adhesive film (13 μm) and polyimide film (7.5 μm) are bonded on the exposed electrodes on both sides. In this step, the pressure is much higher than before, because the adhesive material needs to be squeezed into the spaces between the electrodes. Based on our experiments, for electrodes with a pitch of 200 μm, the pressure should be approximately 2.22 MPa, and for 67 μm pitch electrodes, the pressure should be approximate 2.96 MPa. The pressure should be held for 3 hours at a temperature of 200°C . If the pressure is too low or the curing period is too short, the spaces between electrodes might trap air, and the trapped air is susceptible to electrical breakdown at a lower voltage owing to the low dielectric strength of air.

4.2. Assembly of electrode films and incorporation into actuators

To generate stronger forces, multiple stators and sliders can be stacked. There are two concerns during the stacking process: (1) that the electrodes in different films should be parallel between the stator and slider and should overlap in the same stator/slider; and (2) that the gap between two stacked films should be controlled precisely. If the gap is too small, the friction force between films will be high, whereas a large gap creates a larger distance between electrodes and a diminished driving force.

We developed two methods to overcome these challenges. Our first method is to array the two parts of the actuation area on the same film and fold the whole film to overlap the two actuation areas, as shown in Figure 18. This method can accurately maintain the alignment of the electrodes but does not ensure the thickness of the gap because the actuation section is likely to be curved due to the bending force on the folding edge. Hence, this method is not appropriate for stacking electrode films consisting of more than two sliders/stators. The other method is to use bonding layers to fix the edge of two identical films to make a stator/slider, as shown in Figure 18. In this method, the relative position can be ensured by a frame, and the gap thickness is maintained by carefully selecting the thickness of the bonding layers. These two stacking methods are both utilized in this work.

5. Actuator characterization

To demonstrate the merits of this new design, we fabricated a series of actuators, as shown in Figures 5 and 19, and Tables 2 and 3. These actuators have pitches of 200 μm or 67 μm. The 67 μm pitch actuators correspond to the modeled optimal spacing of 100 μm, as shown in Figure 8. Owing to their stator/slider topology, they can achieve ~50% normalized stroke, which is significantly higher than existing microscale and mesoscale electrostatic actuators; moreover, because of their smaller electrode pitch, they can achieve a higher force per area than centimeter-sized actuators that have a similar air gap between the slider and stator (Figure 2).

5.1. Output force

The actuator driving force was measured and compared with the predicted performance, and the results are shown

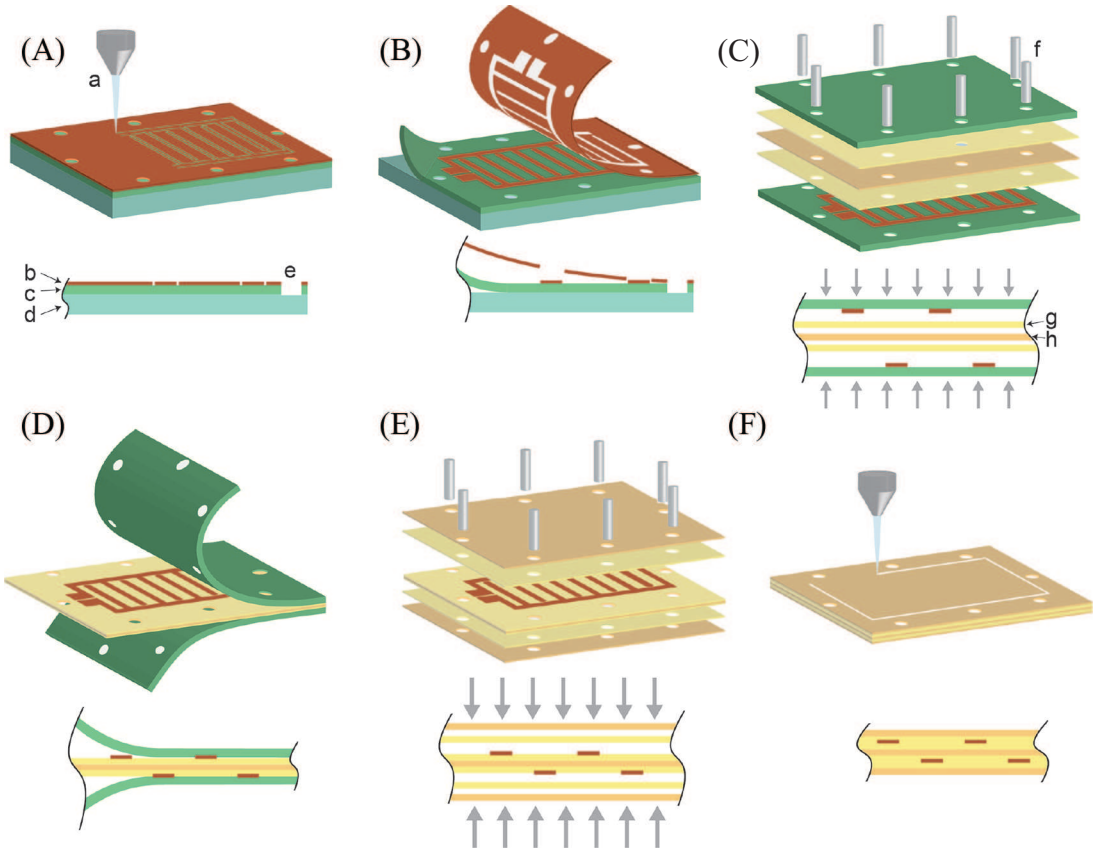

Fig. 17. Overview of the fabrication process. First, we (A) cut the electrodes on the copper sheet using laser ablation and (B) peel off unwanted copper from the adhesive pad. These steps are repeated for both planes of electrodes. Next, we (C) bond the two planes together using heat-curable acrylic adhesive and polyimide film in a pin-aligned heat press, (D) peel off the supporting adhesive pads, and (E) bond dielectric cover layers to the top and bottom. Finally, we (F) release the bonded layers from the substrate using laser ablation. The lowercase letters represent: (a) laser nozzle; (b) copper sheet; (c) adhesive pad; (d) glass slide; (e) alignment hole; (f) alignment dowel pins; (g) thermal adhesive acrylic layer; and (h) polyimide film.

Table 2. Specifications of the electrode films fabricated in this work.

Film	Pitch (μm)	Electrode width (μm)	Thickness (μm)	Area (mm×mm)	Mass (mg)
A	67.1±0.1*	33.3±0.1	72.1±0.3	32.2(±0.2)×5.7(±0.1)	26.1±0.1
B	67.1±0.1	33.3±0.1	72.1±0.2	28.3(±0.1)×5.7(±0.1)	23.2±0.2
C	67.2±0.1	33.3±0.1	71.9±0.3	11.3(±0.1)×7.7(±0.1)	15.2 ±0.2
D	199.8±0.2	100.2±0.2	72.3±0.5	28.2(±0.1)×5.7(±0.1)	22.9±0.2
E	199.6±0.2	100.2±0.1	72.2±0.3	12.1(±0.1)×6.3(±0.1)	12.7±0.2
F**	67.1±0.1	33.3±0.1	72.1±0.3	12.4(±0.1)×18.3(±0.1)	24.1±0.2
G	67.2±0.1	33.3±0.1	71.8±0.2	2.2(±0.1)×5.3(±0.1)	1.7±0.1

*The numbers after the ± symbols are the standard deviation from more than five samples.
**In Film F (a foldable electrode film), there are two identical actuation areas (7.6 mm × 4.6 mm for each).

in Figure 20. The expected quadratic dependence of force on voltage is seen, and the model is verified by the measurements. The coefficients in the estimation are consistent with those listed in Table 1. As estimated in Figure 8, the actuator with smaller spacing generates a stronger force than the actuator with larger spacing. The maximum force generated by a single stator and slider was 15 mN (Actuator 2), and for a stacked actuator was 34 mN (Actuator 6). The estimated value is consistent with these test results. Note that the discrepancy between the modeled and measured output force of the stacked actuators is larger than that of the actuator with only two films. This phenomenon is likely due to uncertainty in the air gap size, as well as misalignment between the films. The output force can be increased further by increasing the effective area. Using longer electrode films than with Actuator 6, a stacked actuator (Actuator 7) can generate a higher maximum force of 85 mN. The force per actuation area of these actuators is 237 N m^{-2},

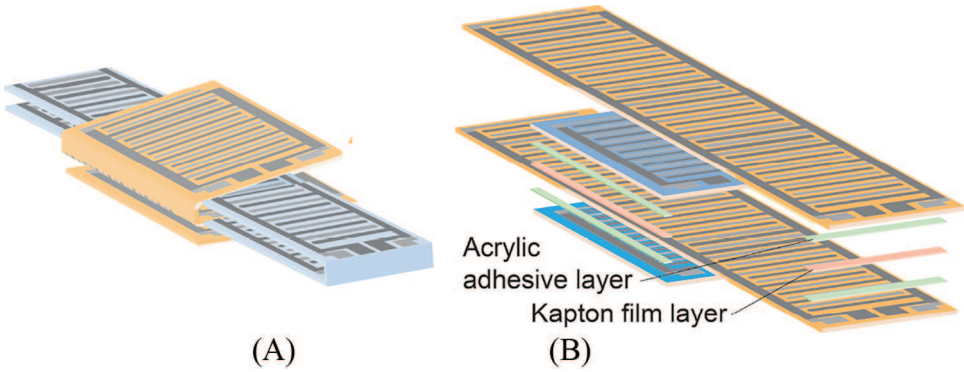

Fig. 18. The assembly methods for multi-layered actuators: (A) origami folding and (B) stacking.

Table 3. Specifications of the mesoscale electrostatic film actuators.

Specifications	Actuator with a single slider and stator				Stacked actuator with multiple films			
Actuator	1	2	3	4	5	6	7	8
Components	2 × Film A	Film B and C	Film D and E	2 × Film G	1 × Film B and 2 × Film C	2 × Film B and 2 × Film C	4 × Film B	Film B and F
Dimension (mm)*	33 × 5.7 × 0.16	28 × 7.7 × 0.16	28 × 6.3 × 0.16	2.2 ×5.3 ×0.16	28×7.7 × 0.25	28 × 7.7 × 0.33	28 × 5.7 × 0.33	28 × 7.7 × 0.25
Weight (mg)	52	38	36	3.4	53	76	92	47
Stroke (mm)	˜15	˜15	˜15	˜3	˜15	˜15	˜15	
Max. speed (mm s^{-1})	—	—	224	—	161	—	—	—
Max. force (500 V)(mN)	34	10	7.0	2	21	34	85	—
Max. output power (mW)	2.2**	—	-	—	—	—	5.6**	—
Power density (W kg^{-1})	42	-	—	—	—	—	61	—

*In the following order: length × width × height. The thickness of the actuators includes air gaps (approximately 15 μm for each).
**This is achieved at driving frequency of 150 Hz.

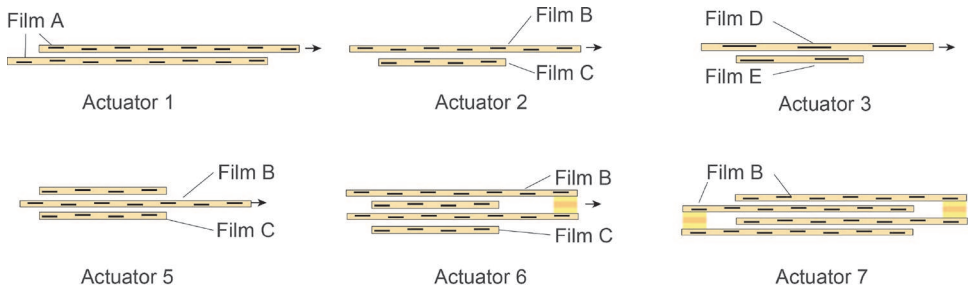

Fig. 19. Schematic of the electrostatic film actuators described in this work. Note that Actuator 8 has the same structure as Actuator 5, except that the two pieces of Film C are replaced by a folded Film F. Actuator 4 has the same structure as Actuator 1, but it is composed of Film G.

more than three times stronger than the previous macroscopic electrostatic film actuators under similar conditions (approximately 78 N m^{-2} in (Wang and Yamamoto, 2013)), as shown in Figure 2.

The driving force as a function of slider speed is shown in Figure 21. Experiments indicate that when the speed is low, the output force is nearly constant, but once the speed exceeds a certain value, the output force starts to fall off linearly to zero. The roll-off in the driving force is likely due to the combined effect of the electrodynamics and a variable coefficient of friction.

5.2. Scalability

To push the performance of small-scale robots, scalable actuators are essential. Based on a hierarchical structure

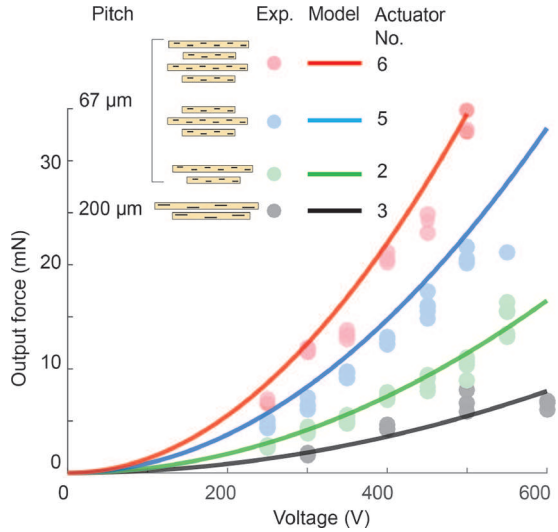

Fig. 20. Output force of different electrostatic film actuators at a driving frequency of 20 Hz. At each condition, there are at least three tests.

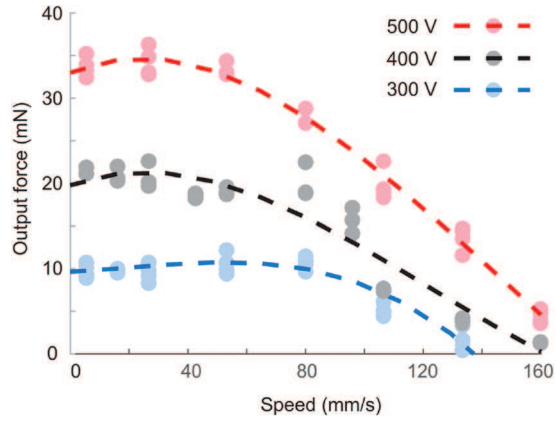

Fig. 21. Output force of the same electrostatic film actuator (Actuator 6) at different speeds. The dashed lines are cubic polynomial fits of the output power at different voltages respectively based on least-squares method. The dots represent the experimental data. At each condition, there are at least three tests.

similar to muscle, the actuators in this work can be easily reorganized and scaled up to satisfy requirements on a large range of output force and sizes. As shown in Figures 22 and 23, the driving force is linearly proportional to the actuation area and the number of stacked actuation interfaces. Thus, we can fabricate actuators with a large range of sizes (as small as 2.2 mm × 5.2 mm in this work), as shown in Figure 6.

5.3. *Displacement and velocity*

The mesoscale electrostatic film actuators operate synchronously, and hence they move at a constant speed if the driving frequency is fixed, as shown in Figure 24. The achievable stroke is quite large: 15 mm for the chosen

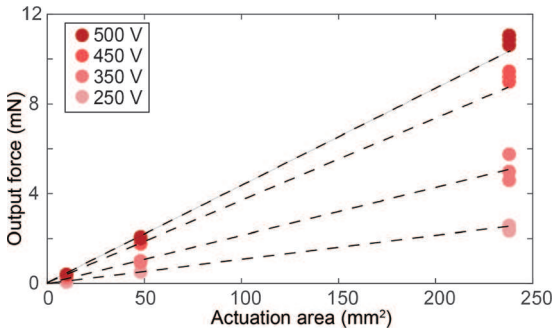

Fig. 22. The variance of output force with respect to the driving voltage. The dots represent the experimental data. At each condition, there are at least three tests. The dashed lines are linear fits of the output force at different voltages, respectively, based on the least-squares method.

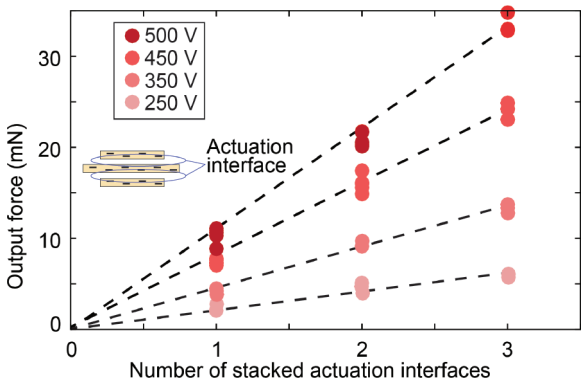

Fig. 23. The variance of output force with respect to the number of stacked actuation interfaces. The dots represent the experimental data. At each condition, there are at least three tests. The dashed lines are linear fits of the output force at different voltages, respectively, based on the least-squares method.

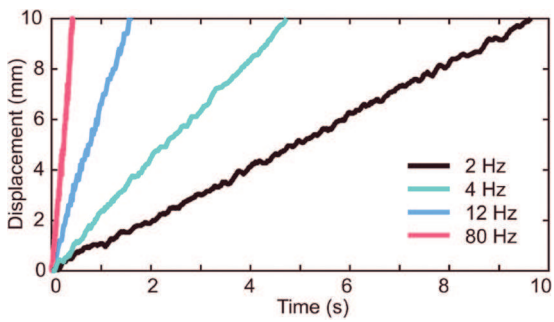

Fig. 24. Displacement of the mesoscale electrostatic film actuator with a pitch of 67 μm (Actuator 2).

geometries. The initial actuator length is 28 mm for Actuators 2–8 (except Actuator 4), which implies a normalized stroke of 54%, far superior to existing mesoscale electrostatic actuators (Figure 2). Note that if the stator is much shorter than the slider, the normalized stroke will approach 100%.

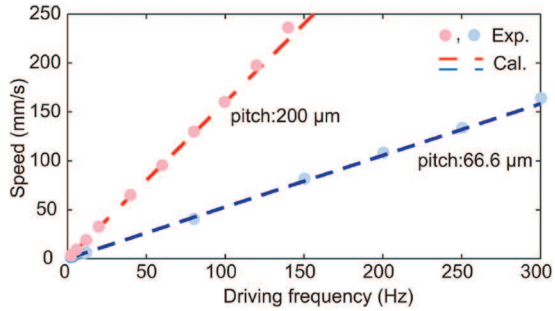

Fig. 25. Speeds for different driving frequencies (Actuator 2, 67 μm pitch; Actuator 3, 200 μm pitch).

Experimental results in Figure 25 show that, as expected (Equation (5)), speed is proportional to driving frequency. The maximum speeds for Actuator 2 and 3 are 161 mm s^{-1} (300 Hz excitation frequency, 67 μm pitch) and 224 mm s^{-1} (140 Hz excitation frequency, 200 μm pitch), respectively. The displacement can be estimated via time-domain integration; a demonstration of open-loop position control of the actuator is shown as Figure 26 (see also Extension 2). The actuator (Actuator 8) attached to a fingernail (for scale) is composed of a long electrode film (the slider) and a folded short electrode film (the stator). When the order of the four phases of the AC supply voltages (400 V_{0-p}, 5 Hz) is reversed after every 3 s, the slider reciprocates with a stroke of 8 mm as shown in Figure 26(B). This demonstration shows that a cyclic motion of the actuator, the basis for simple position control tasks, can be easily implemented.

5.4. *Output power*

The output power can be calculated by taking the product of output forces (mean values of the data at the same operating condition) and the corresponding speed (achieved from the driving frequency by Equation (5)). Both the speed and force contribute to the increase in power output (see the output power of Actuator 1 shown in Figure 27 as an example). Although the force begins to decline for speeds greater than 40 mm s^{-1}, the power continues to grow since the increasing speed is more dominant. Therefore, the optimal speed for the maximum power is greater than that for the maximum force. The power curves are nearly parabolic with peak values of 2.2 mW when the drive signal is 500 V_{0-p}.

As the actuator weighs 52 mg, the maximum power density is 42 W kg^{-1}. This ratio can be increased by stacking more electrode films. For example, Actuator 7, which is formed from four stacked films, has a peak power density of 61 W kg^{-1}, comparable to conventional electromagnetic motors (50–100 W kg^{-1}, including gear reducer, at rated power) (Kingsley et al., 2006) and in the range of mammalian skeletal muscle (50 W kg^{-1} typically and 284 W kg^{-1} maximum) (Kingsley et al., 2006; Madden et al., 2004).

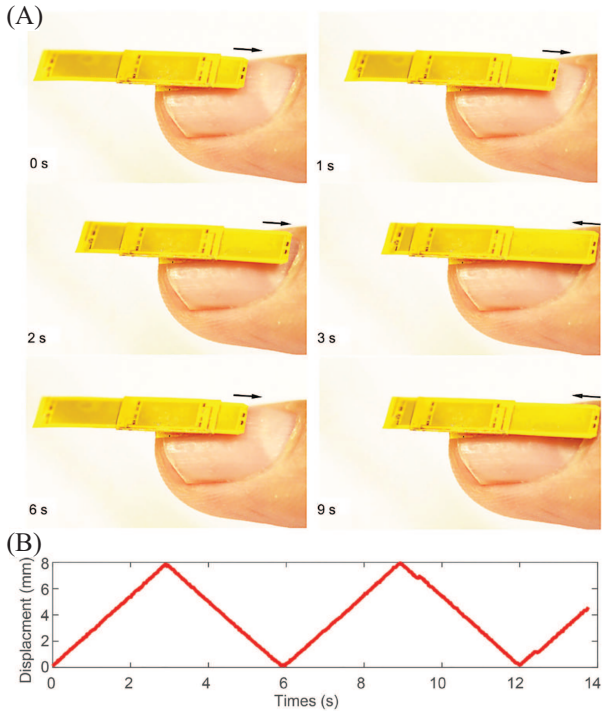

Fig. 26. Open-loop displacement control of the mesoscale electrostatic film actuator by regulating the driving frequency and time duration. (A) Video sequence of actuator cyclic movement based on open-loop control. See Extension 2. (B) The displacement data tracked from the video.

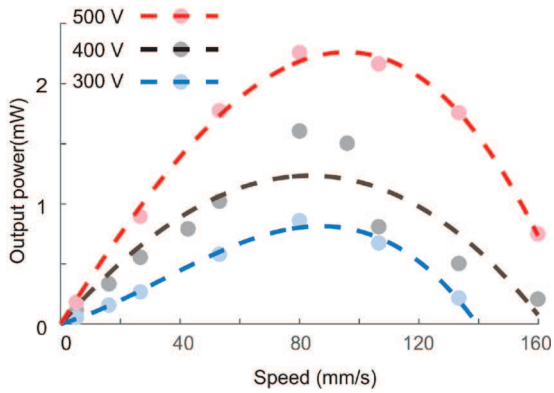

Fig. 27. Mechanical output power at different speeds (Actuator 1). The dashed lines are cubic polynomial fits of the output power at different voltages, respectively, based on the least-squares method.

6. Demonstration of miniature robots integrating mesoscale electrostatic film actuators

With a view toward using these actuators in a wide range of millimeter-scale systems, we present two prototype mesoscale devices with different uses. In both demonstrations, we use Actuator 7. This actuator is thin (0.3 mm) and lightweight (92 mg), can exert a large force (85 mN at 500 V_{0-p}, 20 Hz), and can achieve a peak output power

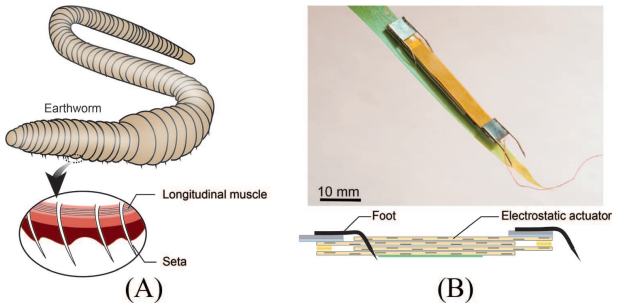

Fig. 28. Comparison of an earthworm and the earthworm-inspired robot. (A) The anatomy of an earthworm. (B) The miniature earthworm robot on a leaf (above) and a diagram of its structure (below).

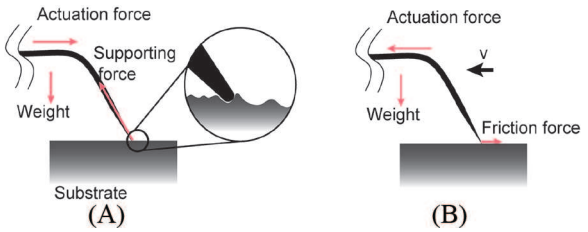

Fig. 29. The asymmetric supporting force of a needle foot. (A) Forces on the foot as the actuation force pushes the foot back. (B) Forces on the foot as the actuator pulls the foot forward.

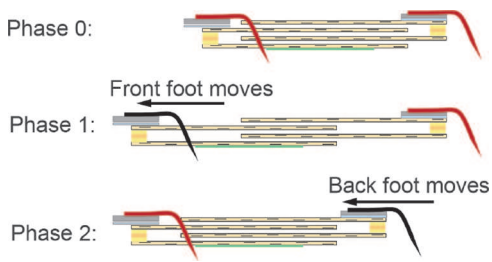

Fig. 30. The earthworm robot's principle of locomotion. The foot is marked in red when it is planted on the ground owing to directional friction.

of 5.6 mW (at 500 V_{0-p}, 150 Hz), as listed in Table 3. To avoid rotational misalignment between the stator and slider films while the actuator operates, a polyethylene terephthalate film is folded into a "U" shape and attached to the stator to act as a guide.

6.1. A miniature earthworm robot

At present, no locomotion method on the mesoscale has achieved the ubiquity of wheeled systems driven by electromagnetic motors on the macroscale. Not only do electromagnetic motors scale poorly to millimeter scales, but efficient transmission systems (consisting of bearings, shafts, and gears) are challenging to fabricate at the millimeter scale. Furthermore, wheeled systems are ill-suited to mesoscale applications, which typically involve cluttered and difficult to navigate environments: search and rescue, pipe inspection, machine maintenance, and so on. To overcome these challenges, researchers have devised systems that use more bioinspired methods of generating motion (Iida and Ijspeert, 2016). One such class of devices are earthworm robots, which move along a surface by sequentially expanding and shrinking their body.

In this work, we devise a bioinspired earthworm robot by imitating the functional longitudinal muscle and seta of earthworms using an electrostatic linear actuator and needles, respectively (see Figure 28). The structure of our earthworm robot is simple: two feet are attached by double-sided tape to both the anterior and posterior edges of the actuator. Each foot is constructed from a rectangular stainless-steel plate (5 mm wide and 7 mm long) and two bent needles (0.4 mm in diameter). The spine feet are inspired by the seta of earthworms. Owing to the angle of spines, the friction force is asymmetric in the forward and reverse directions (Figure 29). The actuator expands and shrinks, like the longitudinal muscles of earthworms. This leads to the simple principle of operation shown in Figure 30 and the stick-slip motion as shown in Figure 31 (see also Extension 3).

Our actuator enables the creation of an earthworm robot with both lower profile and a higher strength-to-weight ratio than existing solutions that use electromagnetic motors, SMAs, and DEAs ((Choi et al., 2002; Duduta et al., 2016; Koh and Cho, 2009; Lee et al., 2015; Lee and Kim, 2008; Lim et al., 2007; Lu et al., 2009; Shian et al., 2015) as listed in Table 4). Piezoelectric polymers (e.g., PVDF) can enable a faster running speed (Wu et al., 2019), but the robot height is greater during movement, and the thrust force is lower than the electrostatic film actuator designed in this work, because its movement depends on bending instead of linear extension. Because of the compact profile (2 mm tall by 7 mm wide) of the electrostatic film actuator, it was able to complete a sample machine inspection task while carrying a small chip-tip camera (Naneye, Awaiba). The task consisted of navigating a 5 mm gap and walking through a wire-filled 19 mm square tube (Figure 32 and Extension 4) to simulate the inspection of an engine. Moreover, because the actuator is composed of compliant parts, it can recover after a deformation caused by an impact. To show the robustness of the actuator to large external forces, we had an adult (weight of 70 kg) step three times on the robot, and we tested the robot between each step. After each step, the robot operated successfully, as shown in Figure 33 (see also Extension 5).

Beyond the simplicity in design and construction, the robot is easy to control. As shown in Figure 31 (data tracked from Extension 3), when the actuator is driven at 10 Hz, and the slider direction is altered every 2 s, the two feet move forward one by one. Although some foot slippage occurs, the relative speed of the slider and stator is constant: 5.2 mm s^{-1} (compared with 5.4 mm s^{-1} as modeled). The average speed of the robot is 1.84 mm s^{-1} (compared with 2.7 mm s^{-1} with no slippage). As the driving frequency increases, the speed of the actuator, and thus the robot, increases. As

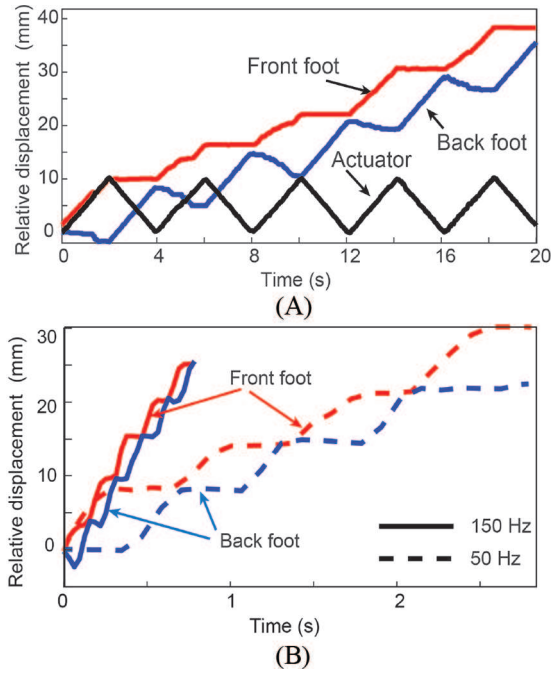

Fig. 31. The displacement of the earthworm robot. (A) The driving frequency is 10 Hz, and the substrate is 2500 grit sandpaper. (B) The driving frequencies are 50 and 150 Hz, and the substrate is 320 grit sandpaper. See Extension 3.

shown in Figure 31(B), at 150 Hz, the robot can move at 26.3 mm s^{-1} (40 mm s^{-1} based on the model, but reduced in practice due to slippage). The slippage occurs since friction cannot stop the moving feet instantaneously. When the robot starts to expand (from locomotion phase 2 to phase 1 as shown in Figure 30), the back feet are expected to stop moving and root at the ground. The feet require a non-zero distance to decelerate. According to Newton's law, larger initial speed results in a longer deceleration distance. In our test, at 150 Hz, the slippage distance of the back feet is 1.6 mm on average, whereas it is only 0.2 mm at 50 Hz. Interestingly, the front feet exhibit a much shorter slippage distance (e.g., 0.07 mm for 50 Hz). This is because during movement, gravity acting on the robot body can cause bending as shown in Figure 34. This bending causes a small tilt angle on the actuation force, which is horizontal initially. The tilted actuating force has an upward component on the back feet and a downward component on the front feet. Consequently, it can reduce the friction force on the back feet and increase the friction force on the front feet, causing the back feet to slip for a longer distance. Similarly, the surface roughness also influences the friction force. In our tests, the robot can barely move on a smooth surface (e.g., 2500 grit sandpaper) owing to substantial slippage. For the future, slippage could be mitigated through modifying the foot geometry by incorporating arrays of sharper needles and/or compliant joints (Asbeck et al., 2006; Lee et al., 2015). Another promising alternative is the use of electroadhesive feet, which can enable climbing on a smooth surface, and even a wall or ceiling (Graule et al., 2016; Wang and Yamamoto, 2017).

In the experiments conducted in this study, the robot was tethered to external voltage amplifiers. However, the robot's high strength-to-weight ratio (369 N kg^{-1}) indicates that it could support a battery, control circuitry, and inspection devices for future autonomous applications using the techniques described in Karpelson et al. (2012). The power consumption is approximately 16 mW, because the current is only 20 μA at its maximum when the voltage is 400 V, as shown in Figure 35. The robot can move for approximately 1 hour and 51 minutes with a miniature battery (GM300910, the smallest known available battery, PowerStream, 8 mAh, 330 mg) (Baisch et al., 2011). Therefore, the cost of transportation is 1.32, calculated by P/mgv (where P is the power, m is the robot mass, and v is the speed). The power consumption and the cost of transportation can be higher if the robot is untethered and more power electronics and control circuits are embedded into its body in the future.

In summary, compared with previous miniature robots driven by different actuators (as listed in Table 3), the earthworm robot presented in this paper has a much smaller cross section (capable of moving through a narrower hole or gap), higher speed, lower mass, and high output force per weight. Owing to the linearity between speed and driving frequency of the actuators, motion control is simple and accurate. Owing to the inherent compliance, the robot is more robust to dramatic disturbances, such as being crushed. This brings the robot closer to natural earthworms, compared with previous rigid miniature robots (Wu et al., 2019). Compared with previous miniature robots that are made of large-scale electrostatic film actuators (Wang and Yamamoto, 2017; Wang et al., 2012), the earthworm robot in this work is much smaller owing to the small size of the driving actuators. Thus, the miniature earthworm robot is much more agile and can navigate a narrow pipe, hole, or crevice.

6.2. *Intestinal smooth-muscle-inspired actuation for a compact endoscopic surgical tool*

Surgical robots require compact actuators for free movement inside confined body cavities. This is particularly relevant in minimally invasive surgical procedures, where flexible instruments are used to reach the surgical target through small incisions or through the natural orifices of the patient's body. Flexible instruments such as endoscopes enable minimally invasive navigation through body cavities (e.g., the gastrointestinal tract). However, their flexibility reduces the achievable dexterity and forces at the tip of the instrument, thus limiting the therapeutic capabilities of current flexible instrumentation. Solutions based on cable-driven mechanisms are currently popular in surgical robotics to actuate manipulation tools at the tip of flexible endoscopic platforms. Nevertheless, their intrinsic

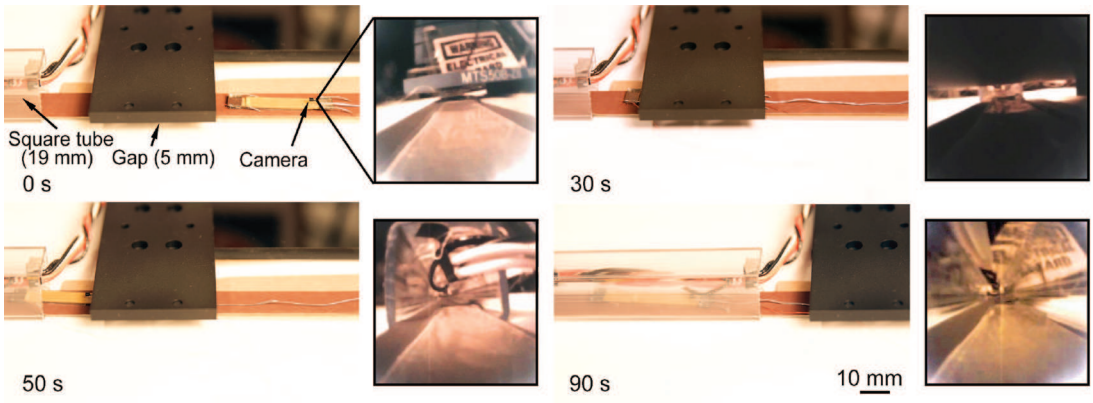

Fig. 32. Image sequence of the earthworm robot traveling through a narrow gap and then a square tube, carrying a chip-tip camera (the camera view is also shown in the inset, see Extension 4).

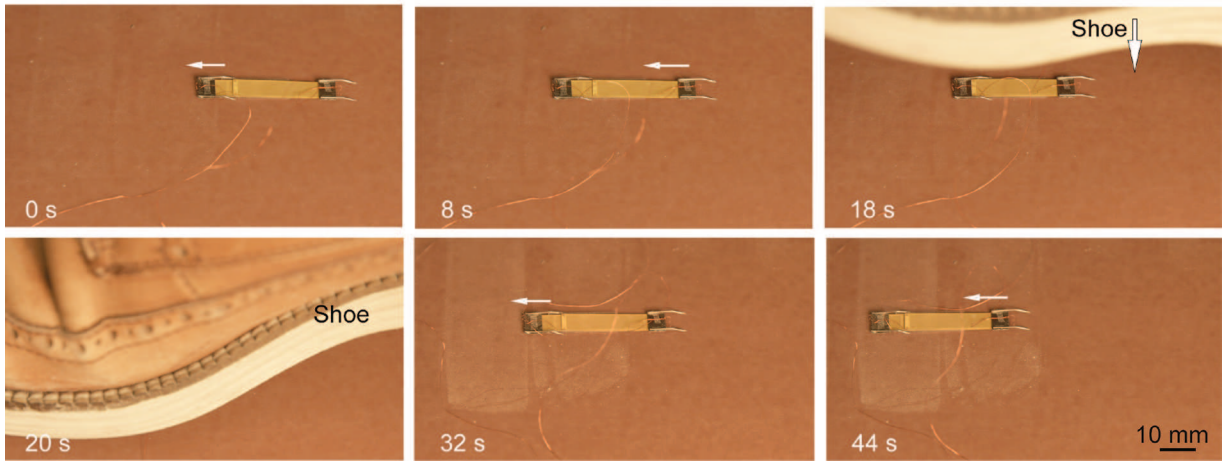

Fig. 33. Locomotion of the earthworm robot before and after being stepped on by an adult (70 kg). See Extension 5.

Table 4. Comparison of miniature earthworm-inspired robots driven by different actuators.

Actuation technique	Robot height[a] (mm)	Speed (mm s^{-1})	Weight (g)	Force per weight (N kg^{-1})
Electromagnetic Oscillatory actuator (Lee et al., 2015)	9	36	2.86	—
Electromagnetic motor (Lu et al., 2009)	7	45	174	14[c]
DEA (Duduta et al., 2016)	10 [b]	20	0.2	—
DEA (Shian et al., 2015)	12	1.1	—	-
DEA (Choi et al., 2002)	30	—	9.7	1.6[c]
SMA (Lee and Kim, 2008)	35	0.57	29	13.8
SMA (Koh and Cho, 2009)	20	5	—	—
Piezoelectric actuator (Wu et al., 2019)	4.2[b]	200	0.024	60[d]
Pneumatic actuator (Lim et al., 2007)	16	48.7	—	—
Electrostatic film actuator (*this work)*	2	26.3	0.23	369[c]

[a]The data are estimated from figures if not reported.
[b]This value is the maximum height during movement.
[c]The force is measured when the robot is suspended in air.
[d]The thrust force per weight is estimated from the payload. The coefficient of friction is assumed to be 0.1.

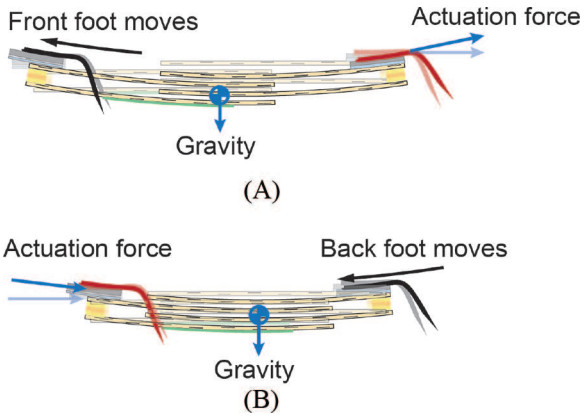

Fig. 34. The robot body bends due to gravity. The portions of lower opacity indicate the initial state of the robot before bending. (A) Bending of the robot body and the force on the back feet in locomotion phase 1. (B) The bending of the robot body and the force on the front feet in locomotion phase 2.

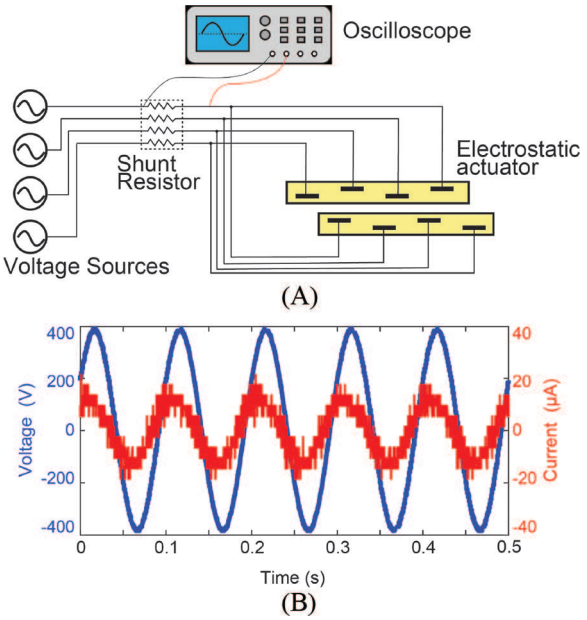

Fig. 35. Depiction of the setup to measure the current of the actuator during operation. (A) The measurement circuit. Each shunt resistor is 2 MΩ. (B) Example of measured voltage and current. The voltage is the value acquired by the red probe of the oscilloscope. The current is the quotient of the voltage across the shunt resistor divided by the resistance.

backlash, low accuracy, and unpredictable failure are bottlenecks to efficient and safe surgical manipulation (Vitiello et al., 2013; Yeung and Gourlay, 2012). SMAs may be another possible solution, but their nonlinearity and hysteresis effects limit their applications (Gafford et al., 2016). In addition, the high temperature generated during actuation may damage the surrounding tissue (Gafford et al., 2017). Recently, a new concept for a hybrid soft/rigid robot mounted to the distal end of conventional endoscopes has been proposed for manipulating endoluminal tissues, but the use of fluidic actuation limits the achievable bandwidth (Becker et al., 2017; Russo et al., 2017).

Millimeter-size electrostatic actuators can be used to generate actuation forces at the tip of an endoscope in a similar way to intestinal smooth muscle, which propels food by contraction and relaxation but takes little space on the intestine, as shown in Figure 36. Our low-profile and compliant actuator can mimic longitudinal smooth muscle by conforming to the exterior of the endoscope with little impact on the maneuverability of the tool, as shown in Figure 37, and its large displacement allows its extensive applications in a variety of contexts. The device's height, displacement resolution, and speed are all superior to previous similar endoscopic add-on tools driven by other on-board actuators, as listed in Table 5. Currently the driving force is designed to be 85 mN, which, although weaker than previous devices, is adequate for cutting and penetration, as shown in Figure 38. It can also be applied to scenarios requiring small forces such as medical inspection (Park et al., 2019). The force can be increased by simply stacking more films and/or increasing the actuation area due to the inherent scalability of the actuator as mentioned in the previous section. A single electrostatic film actuator can be used to drive blades, needles, or forceps in surgical interventions, or multiple actuators could be placed in parallel around a tool to perform coordinated tasks, such as driving a platform containing a camera or other tools (e.g., as a robotic wrist). Here, we demonstrate the cutting and penetration of tissue, using our actuator to drive a blade and needle, respectively. As shown in Figure 38 and Extensions 6 and 7, actuation at the tip of surgical instruments is advantageous for tasks ranging from tissue visualization and resection to suturing or biopsy collection. The actuator can drive either a blade or needle to cut through a piece of chicken breast (approximately 3 mm thick) that is stretched. The speed of the actuator reaches 53.3 mm s^{-1} (100 Hz), which is much faster than common needle insertion speeds (1–10 mm s^{-1}) (DiMaio and Salcudean, 2003), because the actuator directly drives the tools (in contrast to previous cable-driven endoscopic tools which transmit motion through via long path to the distal end from an external motor). Moreover, the average cutting or penetrating speed can be further increased by using a higher driving frequency and/or a shorter stroke. In this experiment, the blade or needle was intentionally actuated to move forward and backward repeatedly. When it was blocked by the tissue, the actuator vibrated automatically with a small stroke, and through the accumulation of these small motions, the tissue was penetrated successfully. In our experiments, a rectangular stainless steel plate was attached with double-sided tape to the slider of the actuator, upon which a blade or needle was affixed via cyanoacrylate glue (Figure 37). The thickness of the blade was 0.08 mm. The needle was 0.4 mm in diameter.

This simple proof-of-concept demonstration illustrates the potential of the actuator to assist with real surgical

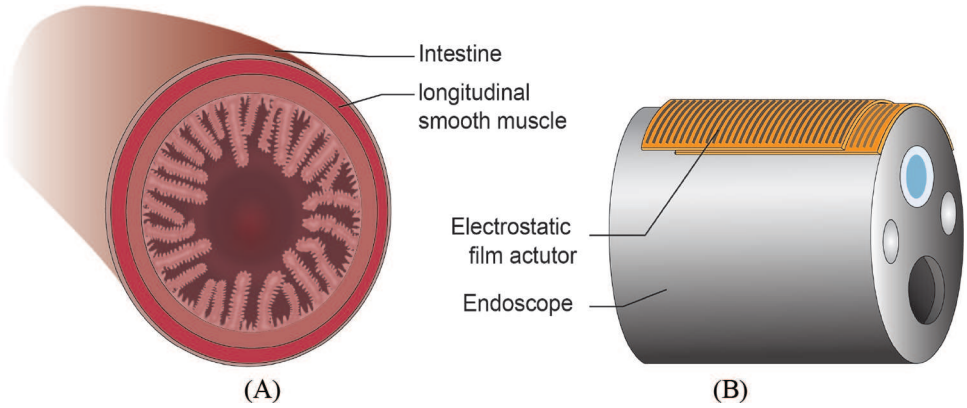

Fig. 36. Comparison of (A) smooth muscle and (B) a thin electrostatic film actuator that conforms and attaches to an endoscope.

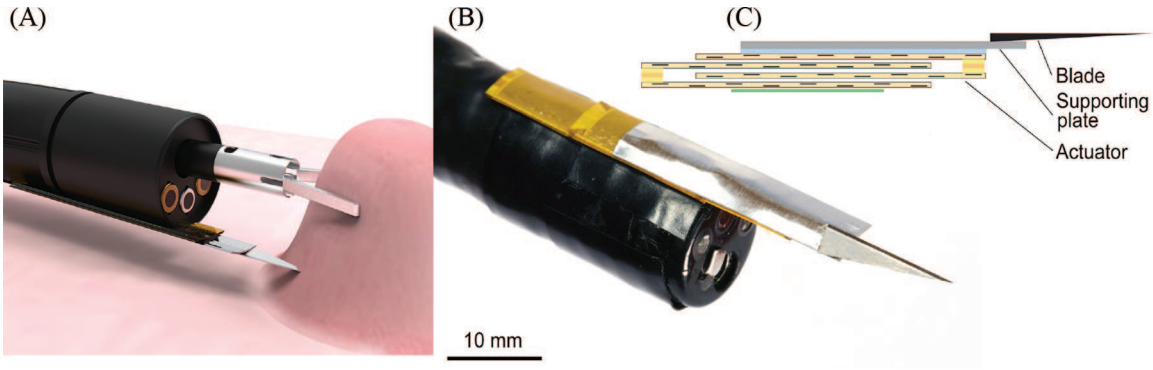

Fig. 37. A low-profile surgical cutting tool based on the electrostatic film actuator. (A) Illustration of a potential application. (B) Photo of the thin and flexible electrostatic film actuator that is bent and mounted on an endoscope to drive a blade. (C) Side view illustration of the low-profile surgical cutting tool.

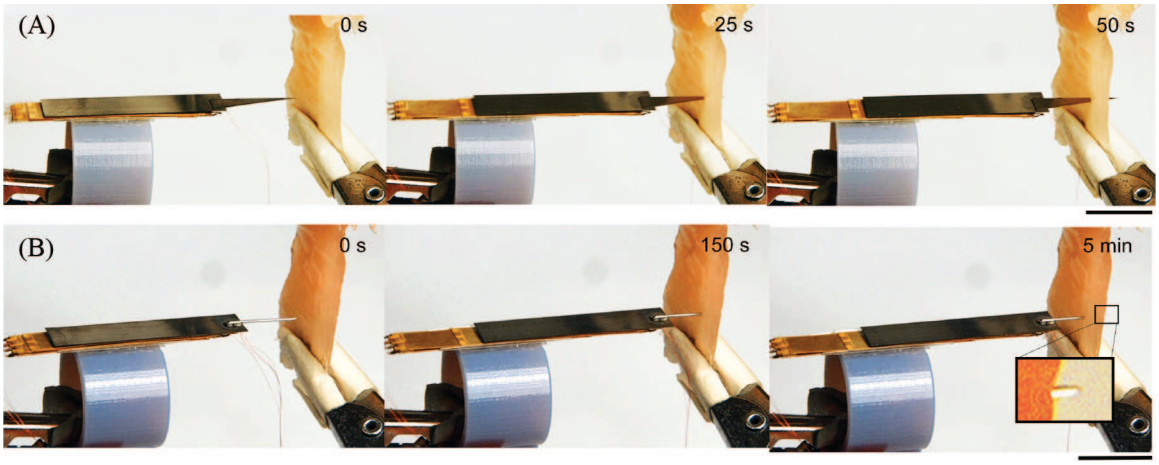

Fig. 38. Demonstration of the cutting/penetrating performance of the low-profile surgical tool based on electrostatic film actuators. (A) Video sequence of cutting a piece of chicken breast (approximately 3 mm thick) with a blade driven by the actuator (see Extension 6). (B) Video sequence of penetrating a piece of chicken breast with a needle (0.4 mm in diameter) driven by the actuator (see Extension 7). Scale bar, 10 mm. The blue 3D-printed ring part represents the distal end of an endoscope.

scenarios: the tissue-cutting task simulates the removal of early stage cancers in the gastrointestinal tract with flexible endoscopes; similarly, the needle-injection task simulates either biopsy collection or injection of saline solution in the submucosa layer of the gastrointestinal tract. The latter is typically performed to elevate the mucosa layer during endoscopic submucosal dissection (ESD) procedures (Maple et al., 2015). In terms of integration, the low-profile actuator can be bent and attached on top of an endoscope (Olympus CF-100L), as shown in Figure 37 (all

Table 5. Comparison of add-on endoscopic surgical tools driven by different on-board actuators.

Actuation technique	Thickness (mm)	Displacement (mm)	Max. speed (mm s^{-1})	Blocking force (N)
SMA (Gafford et al., 2017)	4	8	10	10
Hydraulic actuator (Russo et al., 2017)	1.8 (not inflated)	—	2.8	1.42
Electrostatic film actuator *(this work)*	0.6	15	220	0.085

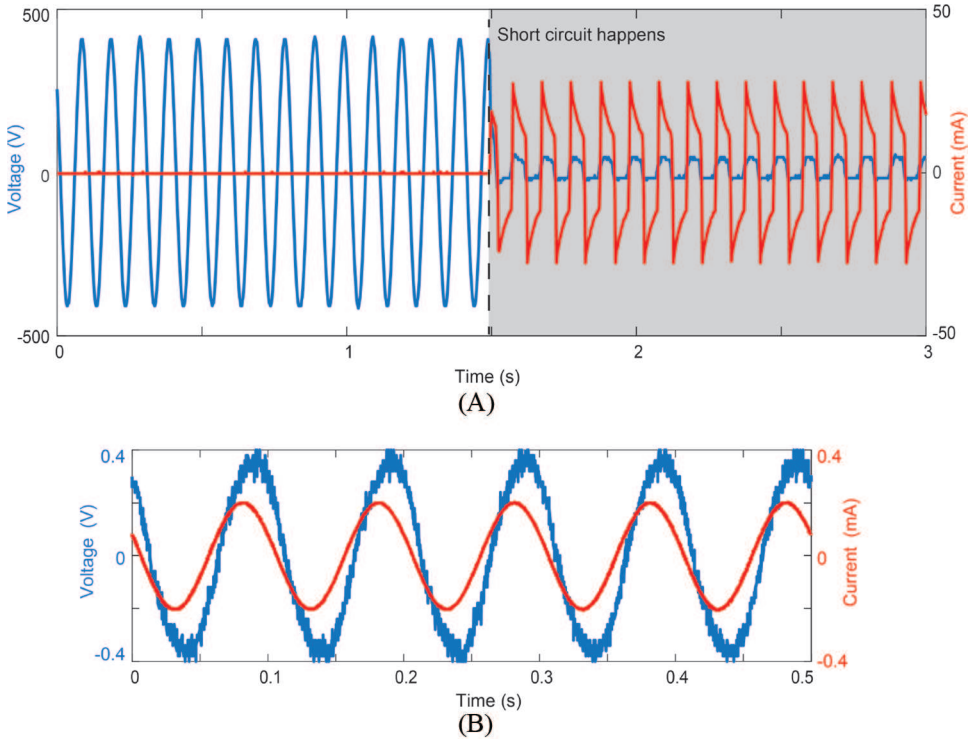

Fig. 39. The influences of a short circuit on the electrical performance of the electrostatic film actuator. (A) The voltage and current on one of the electrode phases before and after a short circuit occurs when no shunt resistor is connected. The current is limited by the amplifier. (B) The voltage and current after the short circuit when a shunt resistor (2 MΩ) is connected.

the components should be covered by an overtube for safety while navigating to the destination). This actuator does not occupy the endoscope working channel, allowing cooperation during surgery with another tool coming out from the working channel and avoiding time wasted on changing tools in the channel (which is quite common in practice).

One of the primary concerns regarding the practical application of mesoscale electrostatic film actuators, particularly in surgical interventions, is the high operating voltage (in our case, up to 500 V). Although this is an understandable concern, we believe that the safety challenges posed by high-voltage operation can ultimately be surmounted. First, all the surfaces of the actuator are covered by a dielectric material (Polyimide, Kapton, with a 146 kV mm^{-1} breakdown strength). Second, other surgical tools have successfully used voltages as high as those used here (Allen et al., 2008; Palanker et al., 2008). For example, electrosurgery applies voltage up to 4,000 V (Suchanek et al., 2016), much higher than the voltage levels used in this work. Lastly, electric current, instead of voltage, poses the primary danger to patients. In our case, the current is much smaller (∼10–100 μA) than the threshold for human perceptibility of 1 mA (Fish and Geddes, 2009). Thus, there is a sufficient safety margin for practical applications. For example, we could set the current limits of the voltage amplifier to be several milliamperes, within the range of safe currents for the human body. Fused drive circuitry could add an additional layer of safety. We conducted a preliminary experiment, scratching off part of the insulation cover layer of the actuator, to verify the ability of our actuators to trigger the current or power limit of the voltage amplifiers used to drive the actuators. As shown in Figure 39, in our test, after the short circuit takes place, the current soars to more than 20 mA from less than 1 mA, and the voltage drops to approximately 40 V from 400 V, owing to the power limitation of the power supplier. We can further set the current to a lower threshold to assure higher safety if required in the future. Moreover, we can connect a shunt resistor in the circuit to

limit the short circuit current. For instance, with a 2 MΩ resistor, the current can be only 0.2 mA at maximum after a short circuit occurs, much lower than the perceptible value of 1 mA.

7. Summary and discussion

Here, inspired by the hierarchical structure of the insect muscle, we have developed and characterized a series of low-profile, large-stroke, lightweight, and flexible mesoscale electrostatic film actuators and applied them to miniature robots. A key contribution is the design, manufacturing, and analyses of the new topology (four-phase two-plane pattern) that allows for easier fabrication and higher performance of electrostatic actuators on the mesoscale. We have fabricated a series of these electrostatic film actuators in different sizes via laser micromachining and precision multi-material lamination. Different experiments show that the actuators can produce forces up to 85 mN and achieve velocities up to 224 mm s^{-1}. The achievable stroke is 15 mm, which corresponds to 50% elongation with respect to the initial actuator length. The displacement and speed of the actuators can be accurately controlled open-loop owing to the linear relationship between speed and driving frequency (quasi-statically).

Here we have demonstrated two applications. First, we have constructed a low-profile miniature robot, inspired by the earthworm, that moves on a level surface and navigates in a narrow gap and, second, we have demonstrated a compact surgical tool that can resect or penetrate tissue with a blade or needle driven by the actuator when mounted an endoscope via imitating the compact and compliant smooth muscle of the intestines.

This paper presents electrostatic actuators for millimeter-scale robots to fill a gap between microscopic and macroscopic electrostatic actuators. Distinguished from other actuators, the present actuators consist of a hierarchical structure including microscale electrodes, electrode arrays, and millimeter stacked layers. Owing to this special structure, the actuators are highly adjustable, more like the nature muscle. For example, the actuator can be reorganized by simply connecting more areas or stacking more electrodes films to tune properties such as stroke, weight, volume, output force, and power for different robots. The actuation principle, models, and fabrication procedure are not limited to the linear actuators described here, but can be extended to a large family of mesoscale electrostatic film actuators with disparate shapes and output motions, including rotary and bending actuators. The insect-muscle-inspired new topology proposed here can also benefit large actuators (tens of centimeters), which is superior to conventional patterns with respect to ease of fabrication and the maximum output force.

Acknowledgements

Authors appreciate Dr. Joshua Gafford and Dr. Hao Su for discussions about potential surgical applications, and Ruth Peña Velasco for her advice on manufacturing. Hongqiang Wang would like to acknowledge the technical support from SUSTech CRF.

Funding

The author(s) disclosed receipt of the following financial support for the research, authorship and/or publication of this article: This work was supported by the Wyss Institute for Biologically Inspired Engineering, the National Science Foundation (award CMMI-1830291), and the Defense Advanced Research Projects Agency (award #FA8650-15-C-7548). In addition, prototype construction was enabled by support from the Army Research Office DURIP program (award W911NF-13-1-0311). Any opinions, findings, and conclusions or recommendations expressed in this material are those of the authors and do not necessarily reflect the views of the National Science Foundation. Hongqiang Wang is partly supported by the National Natural Science Foundation for Young Scientists of China (grant number 51905256), Natural Science Foundation of Guangdong Province of China (grant number 2020A1515010955), and the Science, Technology and Innovation Commission of Shenzhen Municipality (grant number ZDSYS20200811143601004).

ORCID iDs

Hongqiang Wang http://orcid.org/0000-0002-7286-7514
Tommaso Ranzani http://orcid.org/0000-0001-8362-3710

References

Allen PD, Patronik NA, Zenati MA and Riviere CN (2008) A mobile robot driven by miniature onboard motors for cardiac intervention. In: *IEEE Proceedings of the 34th Annual Northeast Bioengineering Conference*, pp. 1117–1124.

Americanpiezo (2020) Piezoelectric ceramics. Available at: https://www.americanpiezo.com/piezo-sale/piezoelectric-ceramics.html (accessed 11 November 2020).

Asbeck AT, Kim S, Cutkosky MR, Provancher WR and Lanzetta M (2006) Scaling hard vertical surfaces with compliant microspine arrays. *The International Journal of Robotics Research* 25(12): 1165–1179.

Baisch AT, Heimlich C, Karpelson M and Wood RJ (2011) Hamr3: An autonomous 1.7 g ambulatory robot. In: *2011 IEEE/RSJ International Conference on Intelligent Robots and Systems*. IEEE, pp. 5073–5079.

Barbarino S, Flores ES, Ajaj RM, Dayyani I and Friswell MI (2014) A review on shape memory alloys with applications to morphing aircraft. *Smart Materials and Structures* 23(6): 063001.

Becker S, Ranzani T, Russo S and Wood RJ (2017) Pop-up tissue retraction mechanism for endoscopic surgery. In: *2017 IEEE/RSJ International Conference on Intelligent Robots and Systems (IROS)*. IEEE, pp. 920–927.

Bell DJ, Lu T, Fleck NA and Spearing SM (2005) MEMS actuators and sensors: observations on their performance and selection for purpose. *Journal of Micromechanics and Microengineering* 15(7): S153.

Birch B (2009) Reliability testing for microvias in printed wire boards. *Circuit World* 35(4): 3–17.

Bloomberg (2020) Price of metals. Available at: https://www.bloomberg.com/markets/commodities/futures/metals (accessed 11 November 2020).

Boys H, Frediani G, Poslad S, Busfield J and Carpi F (2017) A dielectric elastomer actuator-based tactile display for multiple fingertip interaction with virtual soft bodies. In: *Electroactive Polymer Actuators and Devices (EAPAD)* (*Proceedings of SPIE*, Vol. 10163). International Society for Optics and Photonics, 101632D.

Brand RA, Pedersen DR and Friederich JA (1986) The sensitivity of muscle force predictions to changes in physiologic cross-sectional area. *Journal of Biomechanics* 19(8): 589–596.

Burkholder TJ, Fingado B, Baron S and Lieber RL (1994) Relationship between muscle fiber types and sizes and muscle architectural properties in the mouse hindlimb. *Journal of Morphology* 221(2): 177–190.

Carpi F, Salaris C and De Rossi D (2007) Folded dielectric elastomer actuators. *Smart Materials and Structures* 16(2): S300.

Cham JG, Bailey SA, Clark JE, Full RJ and Cutkosky MR (2002) Fast and robust: Hexapedal robots via shape deposition manufacturing. *The International Journal of Robotics Research* 21(10–11): 869–882.

Chen AS, Zhu H, Li Y, Hu L and Bergbreiter S (2014) A paper-based electrostatic zipper actuator for printable robots. In: *IEEE International Conference on Robotics and Automation*, pp. 5038–5043.

Choi H, Ryew S, Jung K, et al. (2002) Microrobot actuated by soft actuators based on dielectric elastomer. In: *IEEE/RSJ International Conference on Intelligent Robots and Systems*, Vol. 2, pp. 1730–1735.

Chu PB, Nelson PR, Tachiki ML and Pister KS (1996) Dynamics of polysilicon parallel-plate electrostatic actuators. *Sensors and Actuators A: Physical* 52(1–3): 216–220.

Cordero F, Craciun F, Trequattrini F and Galassi C (2016) Piezoelectric softening in ferroelectrics: Ferroelectric versus antiferroelectric $PbZr_{1-x}Ti_xO_3$. *Physical Review B* 93(17): 174111.

Costello S, Strusevich N, Flynn D, et al. (2013) Electrodeposition of copper into high aspect ratio pcb micro-via using megasonic agitation. *Microsystem Technologies* 19(6): 783–790.

Diaham S, Zelmat S, Locatelli ML, Dinculescu S, Decup M and Lebey T (2010) Dielectric breakdown of polyimide films: Area, thickness and temperature dependence. *IEEE Transactions on Dielectrics and Electrical Insulation* 17(1): 18–27.

DiMaio SP and Salcudean SE (2003) Needle insertion modeling and simulation. *IEEE Transactions on Robotics and Automation* 19(5): 864–875.

Duduta M, Wood RJ and Clarke DR (2016) Multilayer dielectric elastomers for fast, programmable actuation without prestretch. *Advanced Materials* 28(36): 8058–8063.

Egawa S and Higuchi T (1990) Multi-layered electrostatic film actuator. In: *IEEE Proceedings on Micro Electro Mechanical Systems, An Investigation of Micro Structures, Sensors, Actuators, Machines and Robots.* IEEE, pp. 166–171.

Fish RM and Geddes LA (2009) Conduction of electrical current to and through the human body: A review. *Eplasty* 9: e44.

Fukunaga T, Roy R, Shellock F, et al. (1992) Physiological cross-sectional area of human leg muscles based on magnetic resonance imaging. *Journal of Orthopaedic Research* 10(6): 926–934.

Gafford J, Ranzani T, Russo S, et al. (2016) Snap-on robotic wrist module for enhanced dexterity in endoscopic surgery. In: *IEEE International Conference on Robotics and Automation*, pp. 4398–4405.

Gafford JB, Wood RJ and Walsh CJ (2017) A high-force, high-stroke distal robotic add-on for endoscopy. In: *IEEE International Conference on Robotics and Automation*, pp. 1117–1124.

Goldberg B, Karpelson M, Ozcan O and Wood RJ (2014) Planar fabrication of a mesoscale voice coil actuator. In: *IEEE International Conference on Robotics and Automation*, pp. 6319–6325.

Gonzalez E, Messi M and Delbono O (2000) The specific force of single intact extensor digitorum longus and soleus mouse muscle fibers declines with aging. *The Journal of Membrane Biology* 178(3): 175–183.

Grade JD, Jerman H and Kenny TW (2003) Design of large deflection electrostatic actuators. *Journal of Microelectromechanical Systems* 12(3): 335–343.

Graule M, Chirarattananon P, Fuller S, et al. (2016) Perching and takeoff of a robotic insect on overhangs using switchable electrostatic adhesion. *Science* 352(6288): 978–982.

Gu GY, Zhu J, Zhu LM and Zhu X (2017) A survey on dielectric elastomer actuators for soft robots. *Bioinspiration and Biomimetics* 12(1): 011003.

Hanz B (2020) high quality nitinol nickel titanium shape memory alloy bar rod for sale. Available at: https://www.alibaba.com/product-detail/Shape-Memory-Alloy-Bar-Rod-Buy_1600106631042.html?spm=a2700.7724857.0.0.1c5c18a876FbiJ&s=p (accessed 11 November 2020).

Hassani V and Tjahjowidodo T (2017) A hysteresis model for a stacked-type piezoelectric actuator. *Mechanics of Advanced Materials and Structures* 24(1): 73–87.

Holden H (2009) *The HDI Handbook: A Comprehensive High-density Interconnection Resource for Designers, Fabricators and Assemblers*. BR Publishing.

Iida F and Ijspeert AJ (2016) Biologically inspired robotics. In: *Springer Handbook of Robotics*. Berlin: Springer, pp. 2015–2034.

Jani JM, Leary M, Subic A and Gibson MA (2014) A review of shape memory alloy research, applications and opportunities. *Materials and Design (1980–2015)* 56: 1078–1113.

Josephson RK, Malamud JG and Stokes DR (2000) Asynchronous muscle: A primer. *Journal of Experimental Biology* 203(18): 2713–2722.

Jung K, Nam J and Choi H (2003) Investigations on actuation characteristics of IPMC artificial muscle actuator. *Sensors and Actuators A: Physical* 107(2): 183–192.

Karpelson M, Wei GY and Wood RJ (2012) Driving high voltage piezoelectric actuators in microrobotic applications. *Sensors and Actuators A: Physical* 176: 78–89.

Kedzierski J and Holihan E (2018) Linear and rotational microhydraulic actuators driven by electrowetting. *Science Robotics* 3(22): eaat5643.

Keller S (2014) Webinar hdi microvia technology - cost aspects. Available at: https://www.we-online.com/web/en/index.php/show/media/04_leiterplatte/2014_1/webinare_2/hdi_microvia/Webinar_HDI_-_Cost_Aspects_07012014.pdf (accessed 11 November 2020).

Kha NB and Ahn KK (2006) Position control of shape memory alloy actuators by using self tuning fuzzy PID controller. In: *IEEE Conference on Industrial Electronics and Applications*, pp. 1–5.

King RC and Akai H (1982) *Insect Ultrastructure*, Vol. 1. New York: Plenum Press.

Kingsley DA, Quinn RD and Ritzmann RE (2006) A cockroach inspired robot with artificial muscles. In: *IEEE/RSJ International Conference on Intelligent Robots and Systems*, pp. 1837–1842.

Koh JS and Cho KJ (2009) Omegabot: Biomimetic inchworm robot using SMA coil actuator and smart composite microstructures (SCM). In: *IEEE International Conference on Robotics and Biomimetics*, pp. 1154–1159.

Lau GK, Lim HT, Teo JY and Chin YW (2014) Lightweight mechanical amplifiers for rolled dielectric elastomer actuators and their integration with bio-inspired wing flappers. *Smart Materials and Structures* 23(2): 025021.

Lau JH and Chang C (2000) An overview of microvia technology. *Circuit World* 26(2): 22–32.

Lee Km, Kim Y, Paik JK and Shin B (2015) Clawed miniature inchworm robot driven by electromagnetic oscillatory actuator. *Journal of Bionic Engineering* 12(4): 519–526.

Lee SK and Kim B (2008) Design parametric study based fabrication and evaluation of in-pipe moving mechanism using shape memory alloy actuators. *Journal of Mechanical Science and Technology* 22(1): 96–102.

Legtenberg R, Groeneveld A and Elwenspoek M (1996) Comb-drive actuators for large displacements. *Journal of Micromechanics and Microengineering* 6(3): 320.

Li J, Zhou X, Zhao H, et al. (2017) Development of a novel parasitic-type piezoelectric actuator. *IEEE/ASME Transactions on Mechatronics* 22(1): 541–550.

Lim J, Park H, Moon S and Kim B (2007) Pneumatic robot based on inchworm motion for small diameter pipe inspection. In: *IEEE International Conference on Robotics and Biomimetics*. IEEE, pp. 330–335.

Liu H, Xiong K, Bian K and Zhu K (2017) Experimental study and electromechanical model analysis of the nonlinear deformation behavior of ipmc actuators. *Acta Mechanica Sinica* 33(2): 382–393.

Livermore C, Forte AR, Lyszczarz T, Umans SD, Ayon AA and Lang JH (2004) A high-power MEMS electric induction motor. *Journal of Microelectromechanical Systems* 13(3): 465–471.

Lu H, Zhu J, Lin Z and Guo Y (2009) An inchworm mobile robot using electromagnetic linear actuator. *Mechatronics* 19(7): 1116–1125.

Madden JD, Vandesteeg NA, Anquetil PA, et al. (2004) Artificial muscle technology: Physical principles and naval prospects. *IEEE Journal of Oceanic Engineering* 29(3): 706–728.

Madou MJ (2002) *Fundamentals of Microfabrication: The Science of Miniaturization*. Boca Raton, FL: CRC Press.

Maple JT, Dayyeh BKA, Chauhan SS, et al. (2015) Endoscopic submucosal dissection. *Gastrointestinal Endoscopy* 81(6): 1311–1325.

Martel S (2005) Fundamental principles and issues of high-speed piezoactuated three-legged motion for miniature robots designed for nanometer-scale operations. *The International Journal of Robotics Research* 24(7): 575–588.

Minami K, Kawamura S and Esashi M (1993) Fabrication of distributed electrostatic micro actuator (DEMA). *Journal of Microelectromechanical Systems* 2(3): 121–127.

Mulgaonkar Y, Araki B, Koh JS, et al. (2016) The flying monkey: A mesoscale robot that can run, fly, and grasp. In: *IEEE International Conference on Robotics and Automation*. IEEE, pp. 4672–4679.

Nguyen CT, Phung H, Nguyen TD, et al. (2014) A small biomimetic quadruped robot driven by multistacked dielectric elastomer actuators. *Smart Materials and Structures* 23(6): 065005.

Niino T, Egawa S, Kimura H and Higuchi T (1994) Electrostatic artificial muscle: compact, high-power linear actuators with multiple-layer structures. In: *Proceedings IEEE Micro Electro Mechanical Systems An Investigation of Micro Structures, Sensors, Actuators, Machines and Robotic Systems*. IEEE, pp. 130–135.

Niino T, Egawa S, Nishiguchi N and Higuchi T (1992) Development of an electrostatic actuator exceeding 10 N propulsive force. In: *IEEE Proceedings of Micro Electro Mechanical Systems*. IEEE, pp. 122–127.

Niino T, Higuchi T and Egawa S (1997a) AC dual excitation multiphase electrostatic drive. *Journal of the Robotics Society of Japan* 15(1): 97–102.

Niino T, Higuchi T, Egawa S and Nishiguchi N (1997b) Dual excitation electrostatic stepping motor. *Electrical Engineering in Japan* 119(3): 94–103.

Ning Y (2017) *Reliability of Copper-Filled Stacked Microvias in High Density Interconnect Circuit Boards*. PhD Thesis, University of Maryland.

Palanker D, Vankov A and Jayaraman P (2008) On mechanisms of interaction in electrosurgery. *New Journal of Physics* 10(12): 123022.

Park HC, Zhang X, Yuan W, Zhou L, Xie H and Li X (2019) Ultralow-voltage electrothermal mems based fiber-optic scanning probe for forward-viewing endoscopic OCT. *Optics Letters* 44(9): 2232–2235.

Peek F (1911) The law of corona and the dielectric strength of air. *Proceedings of the American Institute of Electrical Engineers* 30(7): 1485–1561.

Peng Y, Peng Y, Gu X, Wang J and Yu H (2015) A review of long range piezoelectric motors using frequency leveraged method. *Sensors and Actuators A: Physical* 235: 240–255.

Penskiy I and Bergbreiter S (2012) Optimized electrostatic inchworm motors using a flexible driving arm. *Journal of Micromechanics and Microengineering* 23(23): 015018.

Pfahl B, Fu H and Richardson C (2012) Highlights of INEMI 2013 technology roadmaps. In: *35th IEEE/CPMT International Electronics Manufacturing Technology Conference (IEMT)*, pp. 1–5.

Resh VH and Cardé RT (2009) *Encyclopedia of Insects*. Cambridge, MA: Academic Press.

Ricotti L, Trimmer B, Feinberg AW, et al. (2017) Biohybrid actuators for robotics: A review of devices actuated by living cells. *Science Robotics* 2(12): eaaq0495.

Rodgers MS, Kota S, Hetrick J, et al. (2000) A new class of high force, low-voltage, compliant actuation system. Technical Report, Sandia National Labs, Albuquerque, NM, USA.

Russo S, Ranzani T, Walsh CJ and Wood RJ (2017) An additive millimeter-scale fabrication method for soft biocompatible actuators and sensors. *Advanced Materials Technologies* 2(10): 1700135.

Schaler EW, Zohdi TI and Fearing RS (2018) Thin-film repulsive-force electrostatic actuators. *Sensors and Actuators A: Physical* 270: 252–261.

Schindler CB, Greenspun JT, Gomez HC and Pister KS (2019) A jumping silicon microrobot with electrostatic inchworm motors and energy storing substrate springs. In: *2019 20th*

International Conference on Solid-State Sensors, Actuators and Microsystems and Eurosensors XXXIII (TRANSDUCERS and EUROSENSORS XXXIII). IEEE, pp. 88–91.

Sheng J, Gandhi D, Gullapalli RP, Simard JM and Desai JP (2017) Development of a meso-scale SMA-based torsion actuator for image-guided procedures. *IEEE Transactions on Robotics* 33(1): 240–248.

Shian S, Bertoldi K and Clarke DR (2015) Use of aligned fibers to enhance the performance of dielectric elastomer inchworm robots. In: *Electroactive Polymer Actuators and Devices (EAPAD)* (*Proceedings of SPIE*, Vol. 9430). International Society for Optics and Photonics, 94301P.

Suchanek S, Grega T and Zavoral M (2016) The role of equipment in endoscopic complications. *Best Practice and Research Clinical Gastroenterology* 30(5): 667–678.

Sun L, Yu Y, Chen Z, et al. (2020) Biohybrid robotics with living cell actuation. *Chemical Society Reviews* 49: 4043–4069.

Sun M, Huang W, Wang Y, Lu Q and Su Z (2017) Research on a novel non-resonant piezoelectric linear motor with lever amplification mechanism. *Sensors and Actuators A: Physical* 261: 302–310.

Tang WC, Lim MG and Howe RT (1990) Electrostatically balanced comb drive for controlled levitation. In: *4th Technical Digest of the IEEE Solid-State Sensor and Actuator Workshop*, pp. 23–27.

Tang WC, Lim MG and Howe RT (1992) Electrostatic comb drive levitation and control method. *Journal of Microelectromechanical Systems* 1(4): 170–178.

Tang Y, Chen C, Khaligh A, Penskiy I and Bergbreiter S (2014) An ultracompact dual-stage converter for driving electrostatic actuators in mobile microrobots. *IEEE Transactions on Power Electronics* 29(6): 2991–3000.

Tapuchi S and Baimel D (2014) Novel multilayer differential linear electrostatic motor. In: *International Symposium on Power Electronics, Electrical Drives, Automation and Motion (SPEEDAM)*. IEEE, pp. 1368–1372.

Torres J and Dhariwal R (1999) Electric field breakdown at micrometre separations. *Nanotechnology* 10(1): 102.

Trimmer WS (1989) Microrobots and micromechanical systems. *Sensors and Actuators* 19(3): 267–287.

Vitiello V, Lee SL, Cundy TP and Yang GZ (2013) Emerging robotic platforms for minimally invasive surgery. *IEEE Reviews in Biomedical Engineering* 6: 111–126.

Wang H and Yamamoto A (2013) A thin electroadhesive inchworm climbing robot driven by an electrostatic film actuator for inspection in a narrow gap. In: *IEEE International Symposium on Safety, Security, and Rescue Robotics (SSRR)*, pp. 1–6.

Wang H and Yamamoto A (2017) Analyses and solutions for the buckling of thin and flexible electrostatic inchworm climbing robots. *IEEE Transactions on Robotics* 33(4): 889–900.

Wang H, Yamamoto A and Higuchi T (2012) Electrostatic-motor-driven electroadhesive robot. In: *IEEE/RSJ International Conference on Intelligent Robots and Systems*, pp. 914–919.

Webster-Wood VA, Akkus O, Gurkan UA, Chiel HJ and Quinn RD (2017) Organismal engineering: Toward a robotic taxonomic key for devices using organic materials. *Science robotics* 2(12): eaap9281.

Whitney JP, Sreetharan PS, Ma KY and Wood RJ (2011) Pop-up book MEMS. *Journal of Micromechanics and Microengineering* 21(11): 115021.

Wood RJ, Steltz E and Fearing RS (2005) Nonlinear performance limits for high energy density piezoelectric bending actuators. In: *IEEE International Conference on Robotics and Automation*, pp. 3633–3640.

Wu Y, Yim JK, Liang J, et al. (2019) Insect-scale fast moving and ultrarobust soft robot. *Science Robotics* 4(32): eaax1594.

Yamamoto A, Niino T, Ban T and Higuchi T (1998) A high-power electrostatic motor using skewed electrodes. *Electrical Engineering in Japan* 125(3): 50–58.

Yamamoto A, Niino T and Higuchi T (2006) Modeling and identification of an electrostatic motor. *Precision Engineering* 30(1): 104–113.

Yamashita N, Zhang ZG, Yamamoto A, Gondo M and Higuchi T (2007) Voltage-induction type electrostatic film motor driven by two-to four-phase ac voltage and electrostatic induction. *Sensors and Actuators A: Physical* 140(2): 239–250.

Yeh R, Hollar S and Pister KS (2002) Single mask, large force, and large displacement electrostatic linear inchworm motors. *Journal of Microelectromechanical Systems* 11(4): 330–336.

Yen MY, Chiang MH, Tai HH, et al. (2012) Next generation electroplating technology for high planarity, minimum surface deposition microvia filling. In: *2012 7th International Microsystems, Packaging, Assembly and Circuits Technology Conference (IMPACT)*. IEEE, pp. 259–262.

Yeung BPM and Gourlay T (2012) A technical review of flexible endoscopic multitasking platforms. *International Journal of Surgery* 10(7): 345–354.

York PA, Jafferis NT and Wood RJ (2017) Meso scale flextensional piezoelectric actuators. *Smart Materials and Structures* 27(1): 015008.

Zou J and Gu G (2018) High-precision tracking control of a soft dielectric elastomer actuator with inverse viscoelastic hysteresis compensation. *IEEE/ASME Transactions on Mechatronics* 24(1): 36–44.

Appendix A. Index to multimedia extensions

Archives of IJRR multimedia extensions published prior to 2014 can be found at http://www.ijrr.org, after 2014 all videos are available on the IJRR YouTube channel at http://www.youtube.com/user/ijrrmultimedia

Table of Multimedia Extensions.

Extension	Media type	Description
1	Video	Performance of the smallest electrostatic film actuator developed in this work. The size of the actuator is 2.2 mm $\times$ 5.3 mm $\times$ 72 μm.
2	Video	Cyclic movement of a mesoscale electrostatic film actuator. The velocity and displacement are controlled open-loop.
3	Video	Movement of the miniature earthworm robot integrating electrostatic film actuators driven at 10 and 150 Hz.

(Continued)

Cont. Table of Multimedia Extensions.

Extension	Media type	Description
4	Video	The miniature earthworm robot is completing a simulated inspection task in a cluttered environment. It moves through a narrow gap and tube, while carrying a small camera.
5	Video	Robustness test with the miniature earthworm robot. The robot is stepped on by an adult and its performance before and after the impact is shown.
6	Video	Simulation of surgical cutting using the intestinal smooth-muscle-inspired low-profile surgical tool to drive a blade. Human tissue is emulated using a chicken breast. The endoscope is represented by a blue ring.
7	Video	Simulation of a biopsy using the intestinal smooth-muscle-inspired low-profile surgical tool to drive a needle. Human tissue is represented by a chicken breast. The endoscope is represented by a blue ring.

Appendix B. Calculation of actuators with four-phase two-plane electrodes

For the actuator containing electrodes in a single plane, the force can be calculated from Equation (1), and the voltage vector. The capacitances between electrodes in two different films can be represented by

$$\begin{cases} C_{15} = C_{26} = C_{37} = C_{48} = C_{m0} + C_{m1}\cos\left(\dfrac{\pi x}{2p}\right) \\ C_{16} = C_{27} = C_{38} = C_{45} = C_{m0} + C_{m1}\cos\left(\dfrac{\pi x}{2p} + \dfrac{\pi}{2}\right) \\ C_{17} = C_{28} = C_{35} = C_{46} = C_{m0} + C_{m1}\cos\left(\dfrac{\pi x}{2p} + \pi\right) \\ C_{18} = C_{25} = C_{36} = C_{47} = C_{m0} + C_{m1}\cos\left(\dfrac{\pi x}{2p} + \dfrac{3\pi}{2}\right) \end{cases} \tag{12}$$

where p is the electrode pitch, C_{m0} is the mean value, and C_{m1} is the amplitude (which can be calculated via Fourier analysis). These values can be computed from the finite element models.